Global and Planetary Change 220 (2023) 104020

Contents lists available at ScienceDirect

Global and Planetary Change

journal homepage: www.elsevier.com/locate/gloplacha

Allochthonous salt advance recorded by the adjacent *syn*-kinematic sedimentation: Example from the Les Avellanes diapir (South Central Pyrenees)

Gabriel Cofrade [a,*], Irene Cantarero [a], Òscar Gratacós [b], Oriol Ferrer [b], Pedro Ramirez-Perez [a], Anna Travé [a], Eduard Roca [b]

[a] Institut de Recerca UB-Geomodels, Grup de recerca Geologia Sedimentaria, Departament de Mineralogia, Petrologia i Geologia Aplicada, Facultat de Ciències de la Terra, Universitat de Barcelona (UB), c/Martí i Franquès s/n, 08028 Barcelona, Spain

[b] Institut de Recerca UB-Geomodels, GGAC, Departament de Dinàmica de la Terra i de l'Oceà, Facultat de Ciències de la Terra, Universitat de Barcelona (UB), c/ Martí i Franquès s/n, 08028 Barcelona, Spain

ARTICLE INFO

Editor: Zhengtang Guo

Keywords:
Salt sheet emplacement
Sedimentary petrology
Stratigraphy
Fold-and-thrust belt
Southern Pyrenees
Les Avellanes diapir

ABSTRACT

This work aims to present the Les Avellanes diapir as a field analog to inquire how the origin, advance, and emplacement of an allochthonous salt body in continental settings influence the local sedimentation in terms of facies distribution, sediment provenance, and stratigraphic relationships. At the frontal part of the South-Central Pyrenean fold-and-thrust belt (Spain), the Les Avellanes diapir is an outcropping salt structure made of Triassic evaporites, lutites and carbonates. At the diapir's western boundary, a structurally controlled sub-basin presents a well-preserved, early Oligocene in age, mixed clastic-evaporitic sedimentary sequence which recorded the lateral extrusion of the diapir and its emplacement as an allochthonous salt sheet. To define the events and processes recorded by the adjacent sedimentary sequences, and to unravel the diapir evolution and the nature of the diapir contact at the study area, we have combined sedimentary, petrologic, and stratigraphic data. Three stratigraphic sections have been built, from which 8 lithostratigraphic facies associations have been described, interpreted, and correlated across the sub-basin. The deformation within the diapir deposit is also described and interpreted together with the sedimentary rocks. A prograding alluvial to colluvial system is associated with the piercing of the salt, which was exposed at the surface towards the NE area of the sub-basin. The dissolution of the salt resulting in the formation of a caprock with stacks of stringers of intrasalt carbonates and dolerites layers. The ongoing uplifting at the NE caused the incision of the local drainage network, marked as a paleo-relief in the stratigraphic sequence, filled by *syn*-kinematic breccias derived by the erosion, transport, and sedimentation of the caprock. The headward erosion reached the salt underneath the caprock, triggering the lateral extrusion. Thus, salt flowed southwards, favored by the local topography, overriding the *syn*-kinematic breccia deposit. Foliation and other shear-related deformation structures are observed in a megabreccia made of caprock remnants which overlap the sedimentary, *syn*-kinematic breccias along the base of the salt sheet deposit. These structures were probably formed during the advance of the salt sheet. The data acquired and interpreted in this work allows for the conceptualization of the relative lateral movement of a salt sheet front as recorded by adjacent *syn*-kinematic sedimentation in continental settings. Salt supply and erosion rates are compared with topographic slope, sedimentation, and salt dissolution as major controlling parameters of the salt sheet advance. The resulting combinations are expressed by the progradation, aggradation, and retrogradation in terms of proximal over distal facies.

1. Introduction

Allochthonous salt is defined as "subhorizontal or moderately dipping salt, laterally emplaced at a stratigraphic level above the autochthonous source layer" (Hudec and Jackson, 2006). While any subhorizontal salt structure emplaced over younger strata is

* Corresponding author.
E-mail address: gcofrade@ub.edu (G. Cofrade).

https://doi.org/10.1016/j.gloplacha.2022.104020
Received 10 June 2022; Received in revised form 13 December 2022; Accepted 15 December 2022
Available online 21 December 2022

allochthonous by nature, most authors mostly refer to salt sheets or salt canopies as allochthonous, since they are emplaced by the lateral advance of a fluid salt (Talbot, 1998; Talbot et al., 1999; Hudec and Jackson, 2006, 2007; Hearon IV et al., 2015; Závada et al., 2015; Jackson and Hudec, 2017a, Rowan, 2017). In these terms, a salt sheet is an allochthonous mass extruding from a single feeder, while a salt canopy is the amalgamation of two or more salt sheets extruding from different feeders and forming an apparently continuous salt body (Peel et al., 1995).

Despite having been reported in several geological settings, salt sheets and canopies are commonly founded inside collisional orogens (e.g., Iran, Zagros fold-and-thrust belt, Sherkati et al., 2006; or South Australia, Flinders Ranges, Rowan et al., 2019a). This is because the combination of shortening and syn-orogenic deposition usually results in the formation of salt structures or the reactivation of pre-orogenic ones, from which salt may locally extrude (Dooley et al., 2009; Hudec and Jackson, 2006; Callot et al., 2012; Camara and Flinch, 2017; Rowan, 2017; Duffy et al., 2018; Santolaria et al., 2021; Rowan et al., 2022).

In orogenic provinces, salt tends to be accumulated in the front of salt detached fold-and-thrust belts. Prominent examples of allochthonous salt structures within fold-and-thrust belts include the Zagros Salt Province (Talbot et al., 1999; Sarkarinejad et al., 2018; Závada et al., 2021); the Australia Flinders Range (Hearon IV et al., 2015; Rowan et al., 2019a); the Kuqa belt (China) (Li et al., 2014); the Sivas Basin in Turkey (Callot et al., 2014; Legeay et al., 2019); the Katangan Copperbelt in Congo (Jackson et al., 2003); the Alpine Hautte Provence (Graham et al., 2012), or the Basque-Cantabrian basin (Spain) (Carola et al., 2015; Roca et al., 2021) between others. In these areas, the distribution and thickness of salt accumulations strongly affect the structural style (Hudec and Jackson, 2006, 2007; Duffy et al., 2018) which, in turn, influence the regional and local sedimentary record (Andrie et al., 2012; Ribes et al., 2016; Counts et al., 2019). Consequently, the tectono-sedimentary interactions often become increasingly complex compared with the already highly heterogenous *syn*-orogenic sequences located within the fold-and-thrust belts and at the adjacent foreland basins (e.g., Garcés et al., 2020; Calvet et al., 2021). In addition, numerous geological and economic resources are linked to sedimentary rocks associated with salt structures, such as ore deposits, hydrocarbon reservoirs, CO_2 storage, and geothermal reservoirs, among others (e.g., Jackson et al., 2003; Galdos et al., 2019), so the correlation between salt structures and sedimentary processes is an important topic.

The characterization and interpretation of sedimentary sequences adjacent to salt structures, combined with surface and subsurface data, constitute a proven approach for reconstructing salt migration and related deformation along time (Giles and Rowan, 2012; Alsop et al., 2016; Pichat et al., 2019). In the case of extrusive salt sheets (Hudec and Jackson, 2006) the relative movement of the structure can be recorded by the adjacent syn-kinematic sedimentary rocks, so the stratigraphy together with its geometry, offer valuable data to constrain the origin, timing, and mechanisms of allochthonous salt emplacement in an area (McGuinness and Hossack, 1993; Fletcher et al., 1995; Koyi, 1998).

With regard to salt sheet emplacement, there is also a lack of detailed work published on the related sedimentary successions. In contrast, works have been focused on numerical (Pichel et al., 2017; Nikolinakou et al., 2019) and analog (Dooley and Hudec, 2020; Santolaria et al., 2021) modeling of allochthonous salt structures to acquire constraints to be mainly applied in interpretations of non-direct, mostly off-shore collected, geophysical data. Thus, since direct observations are needed to validate numerical and analog models, a necessity arises to find and study field analogs, in order to improve the understanding of the stratigraphic-halokinetic interactions.

In this sense, the salt-detached southern Pyrenean fold-and-thrust belt presents a unique opportunity for the observation between sedimentation, tectonics, and salt related processes. In the south-central part of the Pyrenees (Spain), there are several salt structures piercing through exceptionally well-preserved sedimentary sequences (Vergés et al., 1992; Santolaria et al., 2014; Saura et al., 2016) which record the behavior of salt, along with the development of the fold-and-thrust belt. In recent years, several studies have focused on these salt structures, attempting to explain the role of salt in the Pyrenean orogen formation and evolution (Santolaria et al., 2016; Saura et al., 2016; Camara and Flinch, 2017; Carola et al., 2017; Muñoz et al., 2018; Burrel and Teixell, 2021). Nevertheless, the scope of these studies covers relatively wide areas leading to limited data resolution, which in turn, lead to the simplification of all major outcropping salt structures as vertical diapiric walls (Os de Balaguer map sheet: Teixell and Barnolas, 1996).

To evaluate the understanding of these salt structures and constrain the true shape and nature of salt emplacement, this work focuses on the Les Avellanes diapir, one of the largest within the southern Pyrenees. Adjacent to the western boundary of the diapir, the Os de Balaguer sub-basin infill sequence contains early Oligocene, continental sedimentary rocks apparently overlain by the allochthonous salt, with the mechanism of emplacement being unclear. Therefore, this work aims to uncover the history of the Les Avellanes diapir emplacement by studying the stratigraphy of the surrounding sediments, as well as 1) defining the nature of the diapiric contact in the study area by evaluating the mechanism responsible of the salt emplacement; 2) deducing and locate the history of the diapir piercing, extrusion, and advance; and 3) accordingly reinterpreting the geometry of the western boundary of the Les Avellanes diapir. In addition, the interpretation, distribution, and stratigraphic architecture of the observed facies are used to propose a theoretical, qualitative model that depicts how a continental sedimentary sequence adjacent to an extrusive, horizontally advancing salt sheet changes accordingly to the relative movement of its front, and which factors influence salt movement (McGuinness and Hossack, 1993; Koyi, 1998; Peel et al., 2020). The results presented in this work may be useful as a surface analog for constraining the different stages of salt sheet advance in continental settings, and for other similar basins worldwide.

2. Geological setting

The Pyrenean orogen is an asymmetric, doubly vergent, orogenic wedge located at the north of the Iberian Peninsula (Fig. 1A) which resulted from the continental collision and subsequent subduction of the Iberian Plate under the European Plate from Late Cretaceous to Miocene times (e.g., Muñoz, 1992; Roure and Choukroune, 1998; Teixell, 1998; Vergés et al., 2002; Beaumont et al., 2000; Muñoz et al., 2018; Teixell et al., 2018).

The orogen was built over the inversion of an Early to Late Cretaceous hyperextended margin related to the opening of the North-Atlantic Ocean (Lagabrielle et al., 2010; Angrand and Mouthereau, 2021), and propagated westwards while developing two opposite-verging fold-and-thrust belts (Beaumont et al., 2000). Major convergence rates occurred during the middle Eocene and the Oligocene (Grool et al., 2018; Cruset et al., 2020) decelerating after and lasting in some places until the Miocene (20 Ma.) (Fitzgerald et al., 1999; Huyghe et al., 2012). From late Eocene to the Oligocene, the closure of the foreland Ebro basin, which was previously opened to the North Atlantic Ocean, led to the development of large alluvial fan systems advancing from the central parts of the orogen, which buried most of the south Pyrenean fold-and-thrust belt beneath up to 1.6 km of conglomerate successions (Fillon et al., 2013, Beamud et al., 2010). The burial of the thrust front forced the internal deformation and the out-of-sequence reactivation of the South Pyrenean thrust sheet sequence (Vergés and Muñoz, 1990). During the Miocene, the Ebro basin became opened again towards the SE, to the Mediterranean (Garcia-Castellanos et al., 2003). This opening caused the fluvial incision which exposed most of the southern fold-and-thrust belt pre- and syn-orogenic sequences.

The Pyrenees are structurally divided into a central part, called the Axial Zone, which separates the north and the south fold-and-thrust belts (Muñoz, 1992) (Fig. 1A). The north belt and the Axial Zone are characterized by thick-skinned deformation involving Paleozoic igneous

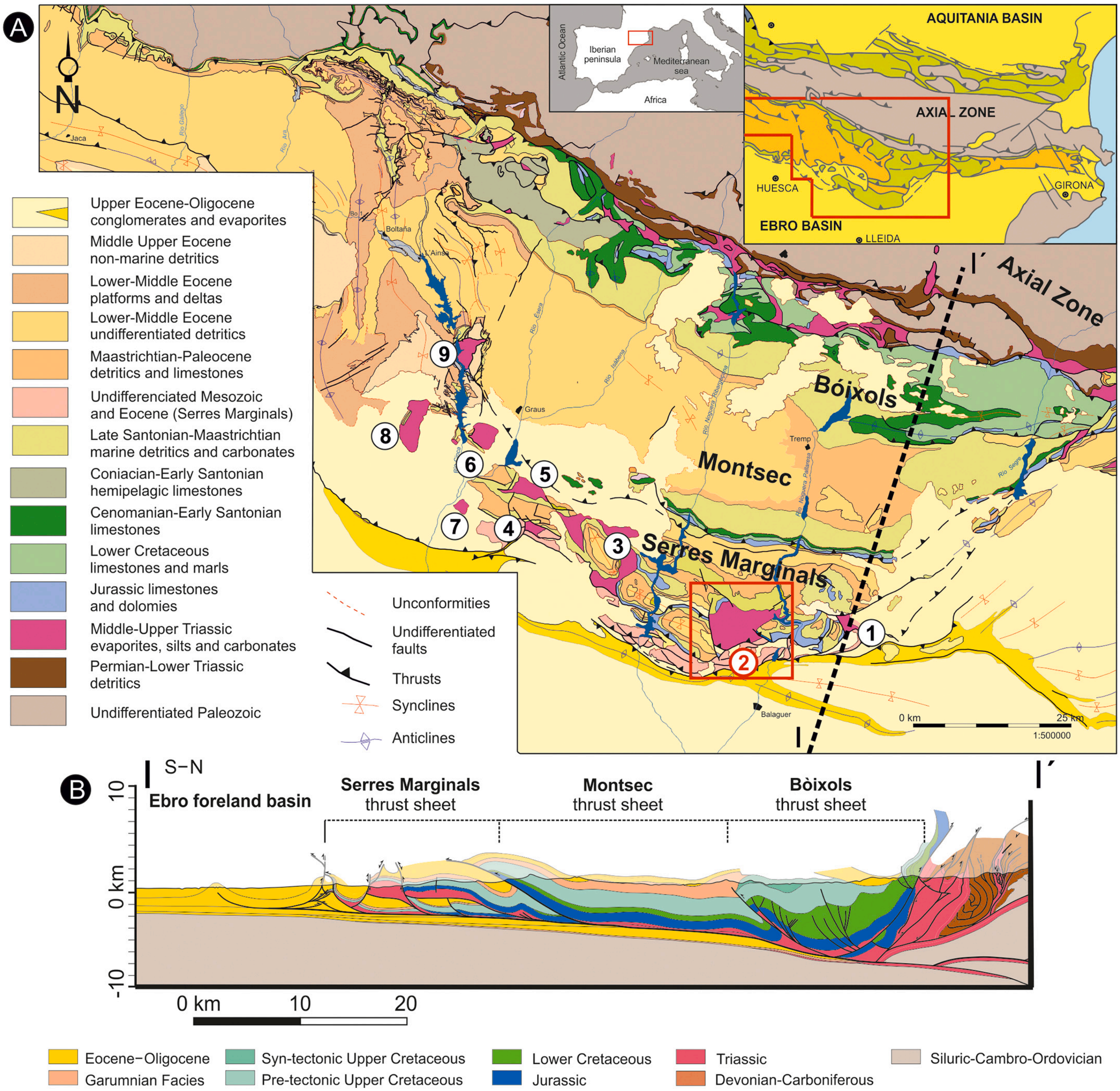

Fig. 1. A: Simplified location maps for the Iberian Peninsula and the Pyrenees, and geological map of the South-Central Pyrenees modified from Muñoz et al. (2018). Red polygons indicate the areas of interest. The name of the three main thrust sheets forming the structural sequence is also located. The numbers refer to salt structures located within the area: 1) Alòs de Balaguer, 2) Les Avellanes diapir, 3) Estopinyà, 4) Calasanz, 5) Justeu, 6) La Puebla de Castro, 7) Estada, 8) Naval diapir, and 9) Clamosa. B: Cross-section of the South-Central Pyrenean wedge. (For interpretation of the references to colour in this figure legend, the reader is referred to the web version of this article.)

and metamorphic rocks imprinted by the Hercynian orogeny, and an attached Mesozoic to Cenozoic sedimentary cover. In contrast, the south belt shows a thin-skinned deformation, and a sedimentary cover detached over the Triassic evaporites. The detached cover is emplaced over the Tertiary sequence of the foreland Ebro Basin with a sole thrust running at the base of the Triassic evaporites (Fig. 1B) (Muñoz, 1992; Beaumont et al., 2000).

The South-Central Pyrenean fold-and-thrust belt forms an arc shaped thrust salient flanked by oblique structures. This area is mainly equivalent to the South-Central Pyrenean Unit defined by Séguret (1972). The thrust salient encompasses three main thrust sheets branching southwards in a piggy-back sequence. These are, from north to south and in order of emplacement: the Bóixols-Cotiella thrust sheet (Late Cretaceous), the Montsec-Peña Montañesa thrust sheet (Paleocene-early Eocene), and the Serres Marginals thrust sheet (lower Eocene-Oligocene) (Fig. 1B). Differential transport displacement along-strike caused the formation of the orogenic curvature in a progressive process controlled by the uneven distribution of the Triassic and Eocene evaporites along the fold-and-thrust belt (Muñoz et al., 2013; Muñoz et al., 2018).

Within the outermost Serres Marginals thrust sheet there are several outcropping major salt structures mainly made of Triassic evaporites linked with orogenic structures, since the Triassic also outcrops in the hangingwall of the thrusts and at the core of the anticline folds, which relate to the salt structures (Fig. 1A) (e.g., Canelles anticline, Salvany, 1999). Several studies have highlighted the link between the distribution of the evaporites with the location, morphology, and development of contractional structures in the area. (Vergés et al., 1992; Sans, 2003; Lopez-Mir et al., 2014; Santolaria et al., 2016; Saura et al., 2016; Camara and Flinch, 2017; Carola et al., 2017; Muñoz et al., 2018; Burrel and Teixell, 2021). Accumulations of Triassic evaporites in the Serres Marginals have been proposed to form in syn-orogenic times mainly by shortening and differential loading (Saura et al., 2016). However, some works have proposed that some salt structures could have started to evolve in pre-orogenic times (Salvany, 1999; Santolaria et al., 2014; Burrel and Teixell, 2021).

2.1. Stratigraphy of the Les Avellanes diapir and its surrounding area

The Les Avellanes diapir is a salt structure made of Triassic evaporites, carbonates and lutites, located in the Serres Marginals thrust sheet (Fig. 1A). The diapir is surrounded by a condensed pre-orogenic and *syn*-orogenic sedimentary sequence ranging from the Triassic to the Oligocene (Fig. 2).

The Triassic in the Pyrenees displays three characteristic facies: the Lower Triassic siliciclastic rocks (Buntsandstein facies), the Middle Triassic carbonates and evaporites (Muschelkalk facies), and the Upper Triassic evaporites and lutites (Keuper facies) (Calvet et al., 2004). The Muschelkalk and the Keuper facies are divided into three intervals each. On one hand, the lower Muschelkalk (M1) is mainly comprised of dolostones, the middle Muschelkalk (M2) of evaporites, and the upper Muschelkalk (M3) of limestones and dolostones (Calvet et al., 1994); and on the other hand, the lower Keuper (K1) is formed of lutites and evaporites, the middle Keuper (K2) of mainly evaporites, and the upper Keuper (K3) of white marls with interlayered dolostones (Calvet et al., 1994; Calvet, 1996; Arnal et al., 2002; Salvany and Bastida, 2004) (Fig. 2). Moreover, intruding into the Triassic succession there are subvolcanic sill-like rocks (dolerites) emplaced during the Upper Triassic (Azambre et al., 1987; Lago et al., 2000).

The late Triassic (Norian-Rhaetian) is represented by dolostones and limestones, named the Isábena formation (López-Gómez et al., 2019; Arnal et al., 2002). This formation is directly overlaid by the Jurassic Lias, Dogger, and Malm units, formed of marine evaporites, carbonates, and marls (Fig. 2).

The Upper Cretaceous is the first syn-orogenic unit in the area. It is divided between a basal Santonian unit, (named Adraén) formed of fluvial quartz arenites and conglomerates (Pocoví, 1978), and an upper Campanian-Maastrichtian unit, (named Calcària de les Serres) made of marine limestones and calcareous arenites (Caus and Gómez-Garrido, 2015) (Fig. 2). The Upper Cretaceous unconformably overlies the Jurassic succession, showing a significant stratigraphic hiatus characteristic of the Serres Marginals sequence. Towards the hinterland, this unconformity disappears, while the Upper Cretaceous shows a transition from shallow to deep marine facies, and a more complete succession (up to 400 m), also overlaying Lower Cretaceous units that are not present in the external parts of the orogen. These relations have been associated with the onset of southward migrating depocenters during the gradual development of the main thrust sequence and the flexure caused by the tectonic loading. The deformation associated with the orogenic building mainly reached the external areas of the fold-and-thrust belt in middle Eocene times, and is thus considered syn-compression (Muñoz et al., 2018) (Fig. 2).

During the transit between the uppermost Cretaceous and the Paleogene, sedimentation progressively changed from marine to continental carbonates, intercalated with fluvial siliciclastic deposits known as Garumnian facies (Cuevas, 1989, Rosell-Llompart, 2001). From the lower Eocene to the Oligocene, sedimentation is mainly controlled by tectonic structures (Fig. 2). The lower Eocene (Ypresian) is represented

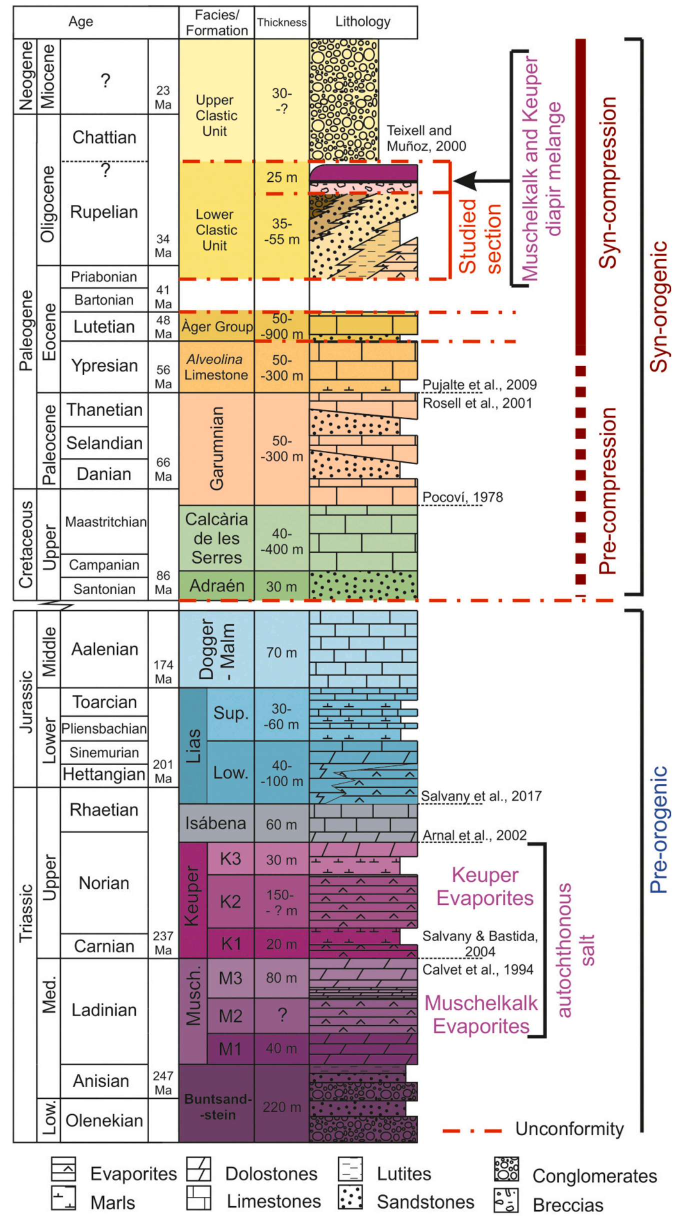

Fig. 2. Stratigraphic column at the study area in relation to Pyrenean deformation. Thicknesses are approximations referred to the Les Avellanes diapir area. Ranges variate considerably since units thicken northwards. Triassic thicknesses are uncertain due to the ductile character of some of these units, so ranges are approximated comparing underground data (Lanaja, 1987; Camara and Flinch, 2017) with stratigraphic studies (Calvet et al., 1994; Salvany and Bastida, 2004; Salvany, 2017).

by grainstones and packstones with *alveolina* and quartz grains, named *Alveolina* Limestones facies (Serra-Kiel et al., 1994, 1998; Pujalte et al., 2009) (Fig. 2).

During the early Oligocene, sedimentation occurred isolated, as structurally controlled sub-basins developed. Teixell and Muñoz (2000) differentiate between two consecutive Oligocene tectonostratigraphic units in the study area either locally deformed by/or post-dating the frontal orogenic thrust units, named unofficially Lower Clastic unit and Upper Clastic unit, respectively (Fig. 2). The Lower Clastic unit encompasses fluvial/alluvial conglomerates mainly formed of Jurassic and Cretaceous rock fragments derived locally from the Serres Marginals erosion. Within the diapir vicinity, these conglomerates change abruptly into mixed clastic-evaporitic successions forming evaporitic packages laterally and vertically confined by conglomerates. One of these clastic-evaporitic successions is the focus of this work (Fig. 2). The progressive increase of metamorphic and igneous clasts in these conglomerates is related to the increasing uplift and subsequent erosion of the Axial Zone during the early to middle Oligocene, and locally marks the transition into the Upper Clastic unit. The deposition of the Upper Clastic unit exceeded the confinement of the local sub-basins, extending regionally as alluvial systems coalesced, a process controlled by the endorheic character of the Ebro Basin during this time (Beamud et al., 2010). Although the upper limit of this unit is eroded in the area, thermochronology models based on apatite fission tracks indicate that conglomerates reached 700 m of thickness in the Serres Marginals (Fig. 2) (Fillon et al., 2013).

3. Methodology

This work is based on structural, stratigraphic, and petrographic data collected in the field mainly in the Os de Balaguer sub-basin. Bedding, joints, faults, and cleavages were systematically measured with a geological compass along a 4-km long, NNW-SSE cross-section, which covers both the diapir deposit and the Oligocene sedimentary infill in the sub-basin. A new geological cartography of the area has been made to reach the desired level of accuracy using the 1:25.000 (Institut Cartogràfic de Catalunya (2010, 2014), and 1:50000 MAGNA series (Os de Balaguer map sheet: Teixell and Barnolas, 1996) as base maps. Figs. 3 and 4 geological maps were also complemented with a digital elevation model covering the study area. This model was constructed with the topographic and elevation dataset provided by the Institut Cartogràfic i Geològic de Catalunya (ICGC), HD-DEM, 2 × 2 m (MET-2) v2.0 (2016–2017) (https://icgc.cat), which is based on airborne collected, 2 m × 2 m resolution, filtered LiDAR data. In addition, PNOA-IGN aerial collected orthoimages available at (https://pnoa.ign.es/), with a maximum resolution of 25 cm/pixel were also used. Both were used for

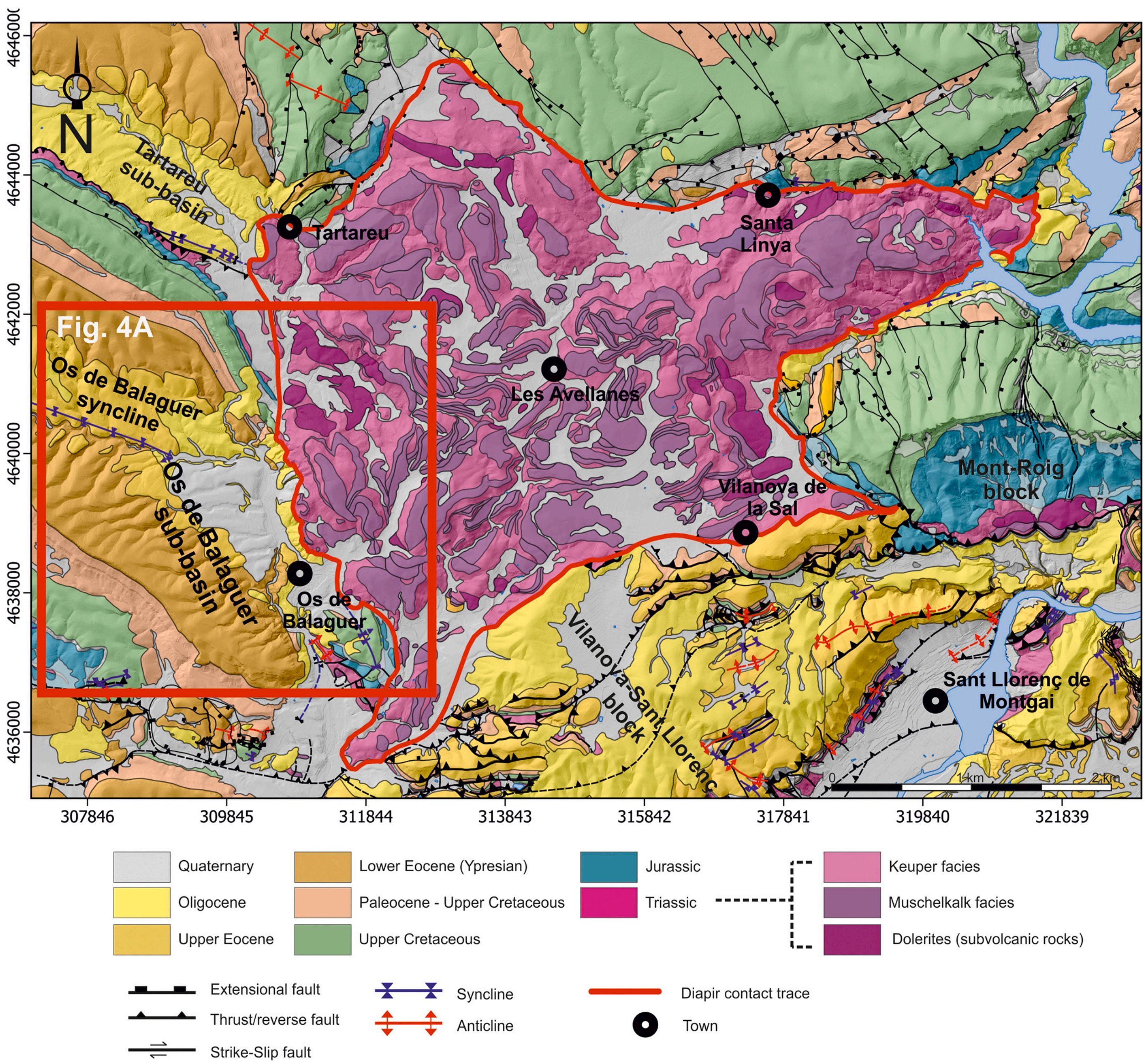

Fig. 3. Geological map of the Les Avellanes diapir. The red square marks the studied area (red rectangle, Fig. 4B). Coordinates are referred to UTM31N, ETRS 89. (For interpretation of the references to colour in this figure legend, the reader is referred to the web version of this article.)

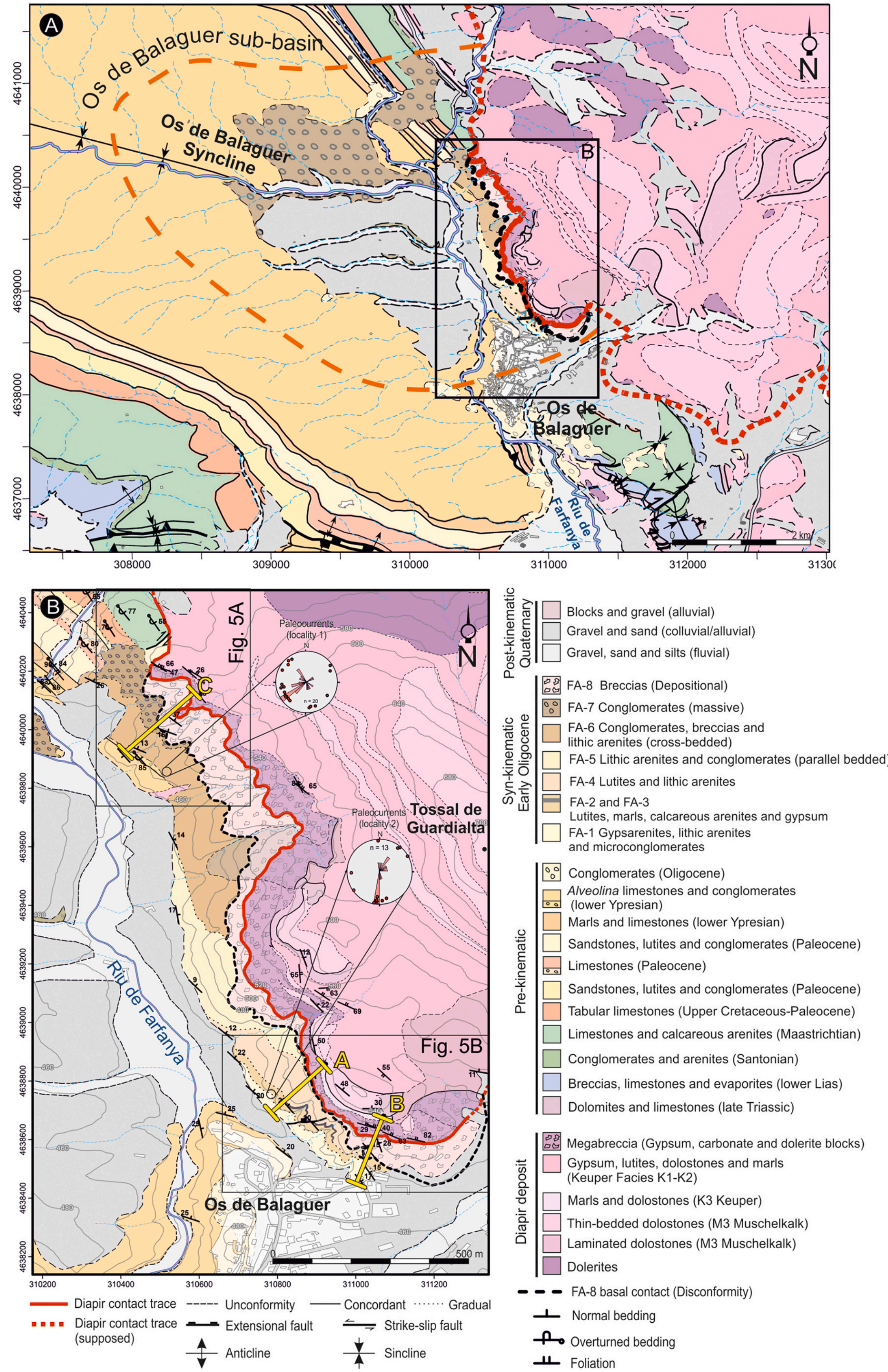

Fig. 4. A: Geological map of the western boundary of the Les Avellanes diapir showing the location of the Os de Balaguer sub-basin. B: Detailed map of the study area and location of the stratigraphic sections A, B, and C. FA: facies associations. See location in Fig. 3. All coordinates are UTM, Z31N, ETRS 89. Roseplots represent the corrected (unfolded) paleocurrent directions acquired from stratigraphic structures on the field. Each plot is a stereographic Lower Hemisphere projection, where n: indicate the number of data plotted in each locality.

mapping improvements such as fine-tuning contacts and supporting structural information, as well as for georeferencing the stratigraphic sections.

Stratigraphic data were collected along the studied profile in selected outcrops with good exposures and vertical and lateral continuity. From north to south, 3 highly detailed stratigraphic sections were constructed. Real thicknesses were measured at each stratigraphic section along the Os de Balaguer profile normal to bed direction with a *Jacob's staff* and a rule to improve precision. Correlations were done projecting the georeferenced sections into a NNW-SSE, 2D correlation panel (approximately following the strike direction), and is also supported by the detailed mapping, and a digital terrain model (DTM). This DTM has been constructed by means of a digital photogrammetry technique extracted from digital image data collected using an unmanned aerial vehicle (DJI Air 2 s model) and processed with the Agisoft Metashape (c) software.

Paleoflows were taken from sedimentary structures (flute marks and clast imbrications) in two different localities and plotted in equal-area Lower Hemisphere stereographic projection after bedding restoration. Roseplots were then created, in which each bar represents a variation in orientation of 10 degrees and the bar length is proportional to the number of measures in each sector (Fig. 4). Stratigraphic data was complemented by petrographic observations using 11 polished thin sections made from representative sampling covering all stratigraphic units. Rock composition was directly described in the field and complemented using petrographic data. From the stratigraphic, sedimentological, and petrographic analysis, 8 facies associations and a diapir unit have been described, mapped, and correlated.

4. Results

4.1. The Les Avellanes diapir main characteristics

The Les Avellanes diapir is an irregular salt structure exposed at the surface as complex arrangement of large, up to kilometer size, truncated bodies of Muschelkalk limestones and dolostones (M3), Keuper laminated gypsum, and dolerites, which are enveloped by the Keuper facies (K1 and K2) (Calvet et al., 1994; Salvany and Bastida, 2004) (Fig. 3). These bodies are stacked, often folded and inverted, resembling a chaotic arrangement in map view. The diapir overburden sequence encompasses from the K3 (Triassic, Norian) to the late Oligocene Upper Clastic unit (Fig. 3).

The diapir surroundings change in structural style from a northern area dominated by extensional faults to a southern area where contractional structures prevail. In the central-western area, there are several NW-SE asymmetric folds in direct contact with the diapir. This area is characterized by kilometer-long synclines, filled by sediments of the *syn*-tectonic Oligocene Lower Clastic Unit, and separated by narrow salt-cored anticlines (Fig. 3).

Two syncline-related sub-basins in the diapir vicinity have preserved comparable Oligocene mixed clastic-evaporitic, syn-orogenic deposits, the northwest Tartareu sub-basin and the Os de Balaguer sub-basin which is the focus of this study (Fig. 3). The age of these sub-basins has not been established by absolute techniques. However, the Tartareu sequence has been dated as early Oligocene through the establishment of biofacies based on charophyte fossil occurrences within the carbonate layers between the evaporites (Ullastre and Masriera, 1999). Furthermore, the same species of charophytes are in the Ebro foreland basin, within a comparable stratigraphic sequence, asserting here the same age. Similar early Oligocene sequences are founded south of the diapir in the Vilanova-Sant Llorenç block (ICGC, 2010) (Fig. 3), which led to the assumption that the evaporitic deposition along the Les Avellanes diapir area occurred broadly at the same time. Since the evaporites are post-dated by the middle-late Oligocene Upper Clastic unit (Teixell and Muñoz, 2000), an early Oligocene age can be assumed for the clastic-evaporitic materials filling the sub-basins along the diapir area.

4.2. The Os de Balaguer sub-basin stratigraphy

The studied early Oligocene sedimentary sequence covers an approximate area of 6 km^2 at the hinge of the Os de Balaguer syncline, a NNW-SSE salt detached fold, plunging eastwards towards the Les Avellanes diapir (Figs. 3 and 4). This sequence onlaps the folded Ypresian limestones in the north and south limbs. It shows thicker successions near the syncline fold axis than at the limbs, as they were structural highs during deposition. These observations suggest that the sedimentation was synchronous with the folding, so the Os de Balaguer sub-basin is therefore interpreted as a structurally controlled sub-basin formed during the development of the Os de Balaguer syncline. This sub-basin is half-elliptical shaped, with an NW-SE major axis of 4 km in length and a minor axis of 2 km (Fig. 4A).

The sedimentary part of the sequence is composed of 8 Facies Associations (FA-1 to FA-8), which consistently dip towards the NE and lie unconformably over the Ypresian limestones. In the north, the sequence postdates the overturned pre-Oligocene units (Fig. 5A) while in the south, it onlaps the NE dipping *Alveolina* Limestones. Except for the boundaries between FA-3 and FA-4, which are sharp and concordant, facies from FA-1 to FA-7 mainly present gradational boundaries, laterally and vertically changing facies (Figs. 4B and 5). FA-1 to FA-4 appear at the base of sections A and B (Fig. 6) and only outcrop at the SSE part of the sub-basin (Fig. 5A). FA-5 outcrops at the lower middle part of the studied profile (Fig. 4B) and represents a transitional unit between FA-4 and FA-6. FA-6 to FA-7 are in section C (Fig. 6) and only outcrop at the NNE of the sub-basin (Fig. 5A). FA-8 is present in the three sections and unconformably overlies all the previous facies (FA1 to FA-7) (Figs. 4B, 5, 6).

The diapir contact is represented on the map by a red trace (Fig. 4B). It displays an irregular geometry along the studied profile, being subhorizontal in the northern area, and smoothly dipping towards the NE in the southern area (Fig. 4B). The diapir contact is concordant with the bedding of the sedimentary layers below it, and therefore, the diapir does not intrude vertically, and instead lie on top the sedimentary facies (Fig. 5).

4.3. Description of the Facies Associations

The 8 Facies Associations (FAs) in the Os de Balaguer sub-basin (Figs. 4, 5, and 6) are presented below. From bottom to top:

FA-1: Gypsarenites with lithic arenites and microconglomerates (Fig. 6, sections A, and B, and Table 1). This FA is formed by an alternation of laminated gypsarenites with lithic arenites and microconglomerate layers in a thickening upwards sequence (Fig. 7A, D). Gypsarenites show a characteristic planar-parallel lamination made of gypsum-rich layers alternating with silty layers, arranged in depositional sets. Sets rhythmically vary in thickness from thin (around 1 mm) to thick (several mm) revealing a fine depositional cyclicity. In these sets, centimeter tepee-like structures are rather common (Fig. 7A). Numerous centimeter-sized lenticular gypsum crystals are present and concentrated in some stratigraphic levels disrupting the lamination (Fig. 7B).

Lithic arenites and microconglomerates are arranged into slightly planar-convex, normal graded, centimeter to meter-thick beds. Small flute marks at the base of these beds (Fig. 7C) indicate the presence of north to south paleocurrents (Fig. 4B). Grain size rapidly decreases upwards from microconglomerates to medium to fine arenites with small-scale trough cross-bedding, pointing to a rapid deceleration in transport energy. Microconglomerate composition mainly consists of Muschelkalk carbonates, dolerites and other carbonate rock fragments from the overburden units, as well as monocrystalline quartz fragments (Fig. 7D).

FA-2: Lutites with intercalated tabular gypsum beds (Fig. 6, sections A and B, and Table 1). This association encompasses an alternation between dark planar parallel laminated lutites with centimeter thick, tabular, alabastrine gypsum beds. Depositional structures are not

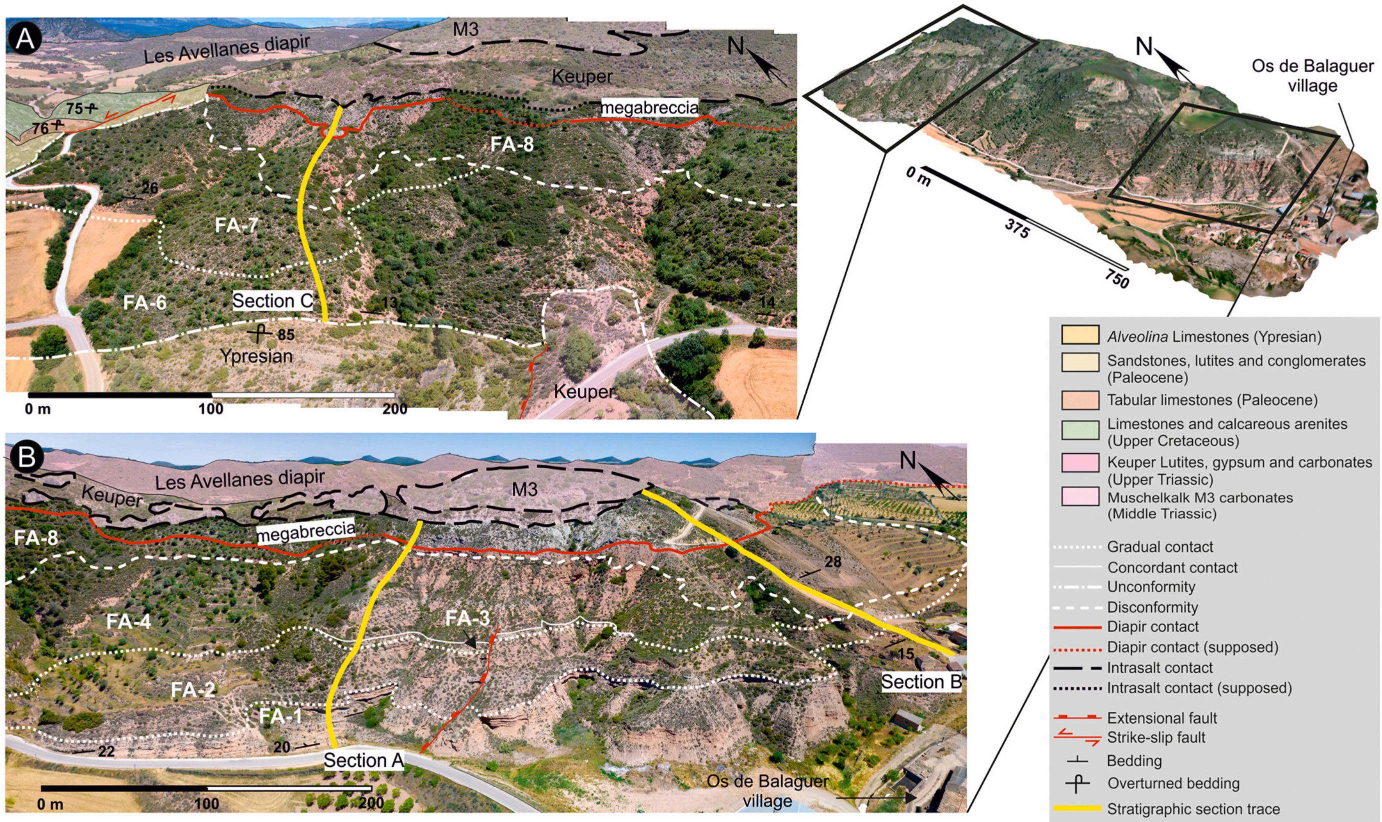

Fig. 5. Outcrop views of the studied profile (3D stereographic model made through aerial photographic composition). A: NNW area where section C is located. B: SSE area where sections A and C are located. See Fig. 4B for the exact location of the images.

recognizable in gypsum beds (Fig. 7E). The FA-1 evolves progressively into FA-2 (Fig. 5B).

FA-3: Calcareous arenites and marls (Fig. 6, section A, and Table 1). This FA consists of a marly interval with fine calcareous quartz-rich lithic arenite beds intercalated at its central part. These arenites show small-scale trough cross-bedding with marls intercalated within foresets, defining flaser textures that transitionally evolve vertically into more pure sand intervals towards the top (Fig. 7F). Small-scale trough cross-bedding is randomly oriented, and it was not possible to determine the paleoflow direction. FA-3 wedges laterally along-strike (Figs. 4 and 5B).

At microscale, arenites depict an alternation between very clean, open-porosity laminae, and intervals richer in silty components. The arenite-rich layers are well-sorted and are mainly composed of millimeter-sized, subangular quartz grains (Fig. 8A). Muscovite and biotite grains are also present and appear deformed by mechanical compaction. Lutites are mainly formed of red-colored clay minerals and micrite, with scarce quartz grains.

FA-4: Lutites and lithic arenites (Fig. 6, section A, and Table 1). This association is mainly formed of reddish planar-parallel laminated sandy lutites (Fig. 7G) intercalated with tabular, centimeter thick, lithic arenite beds (Fig. 7H). Some of these beds have a basal lag of pebbles and slightly erosive bases. Lithic arenites are composed of carbonates (mainly from the Muschelkalk), dolerites, and quartz grains (Fig. 8B). Arenite beds present little amounts of matrix and show minor carbonate cementation, so the interparticle porosity remains largely open and interconnected. Quartz grains show pressure contacts indicating mechanical compaction. At the SE of the Os de Balaguer sub-basin, the FA-4 presents a net base concordant with the FA-3 (Fig. 5B) and changes laterally northwards into FA-6 (Fig. 4B).

FA-5: Parallel bedded lithic arenites and conglomerates (Fig. 9A, and Table 1). The FA-5 is represented by reddish conglomerates and arenites organized in parallel-bedded centimeter thick beds. Conglomerate beds normally show slightly erosive bases with basal pebble lags, evolving upwards into medium to coarse arenites. The arenites may present rough small-scale trough cross-bedding. Clasts are mainly of Muschelkalk carbonates and dolerites, being also present detrital gypsum clasts, minor components of *Alveolina* Limestone fragments, monocrystalline quartz, and micas (Fig. 9B). The gypsum clasts are well-rounded and moderately sorted, contrasting with the subangular Muschelkalk carbonate and dolerite fragments. FA-5 has not been represented in any stratigraphic section due to a lack of continuous outcrops. FA-5 evolve laterally and vertically into FA-6 (Fig. 4B).

The FA-5 to FA-8 sequence displays a pervasive secondary gypsum cement form of poikilotopic, anhedral in shape, 1–10 mm crystals of gypsum with some anhydrite inclusions (Fig. 8C and D). Matrix is formed by fine lutites, and it is relegated to pockets in between gypsum crystal boundaries and inclusions within the large crystals (Fig. 8C). Some angular quartz fragments present in these facies also contain anhydrite inclusions (Fig. 8E). Clasts have small, millimeter to centimeter thick fractures filled with a fibrous gypsum cement also associated with short, millimeter to centimeter thick veins subparallel to bedding (Fig. 8G).

FA-6: Cross-bedded conglomerates, breccias, and lithic arenites (Fig. 6, section C, and Table 1). These facies are composed of lithic arenites and conglomerates arranged in meter-scale sets with cross-bedding. Sets are normally graded with imbricated basal lags made of subangular blocks and clasts evolving upwards into trough cross-bedded sandstones and microconglomerates (Fig. 9C). Imbrications were used to measure paleocurrent sense, obtaining a mean NW to SE direction at the NNW part of the studied area (Fig. 4B) Grain composition shows predominantly Muschelkalk carbonates, dolerites, and *Alveolina* Limestones fragments as well as other local-derived calcareous rock fragments (mostly from the Mesozoic) (Fig. 9C). Subrounded alabastrine gypsum

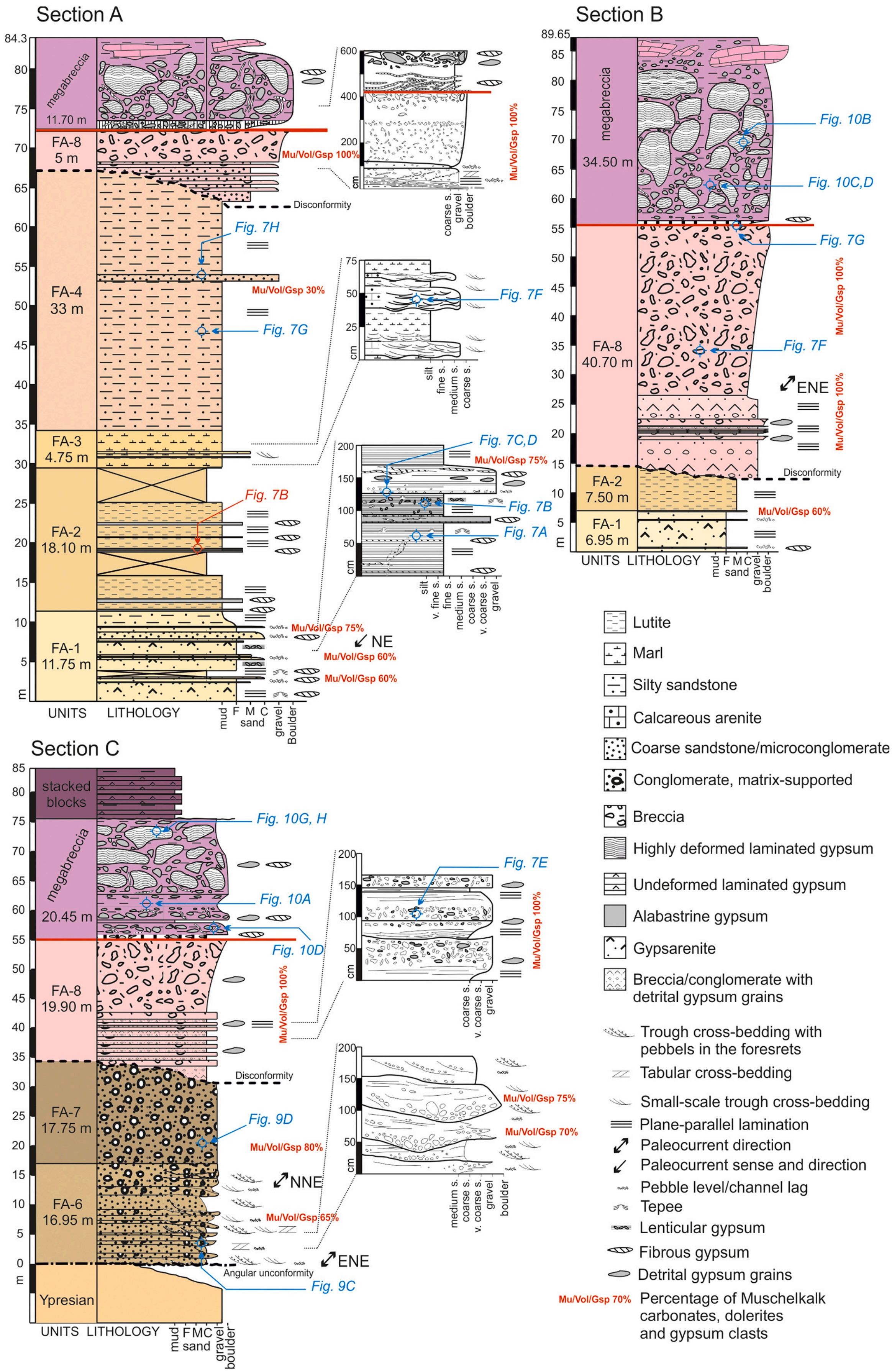

Fig. 6. Stratigraphic sections A, B, and C. See location in Figs. 4B and 5.

Table 1
Summary of the Os de Balaguer sub-basin sedimentary facies associations and its associated depositional environments. Abbreviations: f. fine, m. medium, c. coarse.

Facies Association	Facies	Lithology	Sedimentary structures	Geometry	Depositional processes	Depositional environment
FA-1	Facies 1.1	Gypsarenites and lithic arenites (m., f.)	Plane-parallel lamination, tepees	Tabular	Evaporitic deep lacustrine deposits	Saline lake (deep)
	Facies 1.2	Lithic arenites (m., c.) and microconglomerates	Flute marks	Tabular to lenticular	Discharge lobules	
FA-2	Facies 2.1	Black lutites, alabastrine gypsum interlayered	Plane-parallel lamination	Tabular	Evaporitic margin deposits	Saline lake (margins)
FA-3	Facies 3.1	Calcareous arenites (m.) and marls interlayered	Small-scale cross-bedding (ripples)	Tabular to plano-convex	Mixed aeolian--lacustrine shoreline	Saline lake (shoreline)
FA-4	Facies 4.1	Sandy lutites	Plane-parallel lamination	Tabular	Overbank	Fluvial/ distal alluvial
	Facies 4.2	Arenites (m.)	pebble lag	Tabular	Amalgamated sandy channels	
FA-5	Facies 5.1	Lithic arenites (f., m., c.) and conglomerates	Parallel bedding, pebble lags, ripples	Tabular to channelized	Non-to-slightly channelize alluvial flow	Alluvial (intermediate)
FA-6	Facies 5.2	Conglomerates, breccias, and lithic arenites (m., c.)	cross-bedding, pebble lags, ripples	Trough crossbeds	Amalgamated channels	Alluvial (proximal)
FA-7	Facies 7.1	Conglomerates	massive	Very crude layering	Colluvial deposits	Alluvial (proximal) to Colluvial
FA-8	Facies 8.1	Breccias	cross-bedding, pebble lags	Trough crossbeds	Amalgamated channels	Alluvial (proximal)
	Facies 8.2	Breccias	Parallel lamination, accretion planes	Cross-bedded to massive	Colluvial deposits	Alluvial (proximal) to Colluvial

clasts as well as rounded mono- and polycrystalline quartz grains and quartzite rock fragments are present. FA-6 laterally changes northwards into the FA-7 facies at the N of the Os de Balaguer sub-basin (Fig. 5A).

FA-7: Massive conglomerates (Fig. 6, section C, and Table 1). This FA is mainly composed of massive conglomerates and breccias with a very coarse sand matrix and gravel to boulder size floating clasts. Matrix-rich intervals alternate with gravel-rich intervals showing crude parallel bedding with poorly defined boundaries. A very crude thinning-upwards general trend is observed. Composition is similar to the observed in FA-6. Vertically and laterally these conglomerates rapidly change to FA-6 and FA-5, which define a wedge-like shape for these deposits (Fig. 6B).

FA-8: Breccias (Fig. 6, sections A, B and C, and Table 1). The FA-8is a mud-supported, poorly sorted, depositional breccia made of clasts and blocks of Muschelkalk carbonates, dolerites, and rounded detrital gypsum grains floating in a fine reddish lutite matrix. The presence of high percentages of detrital gypsum clasts within the sediment stands out.

The breccia changes in facies vertically. At the base, there is an association of amalgamated beds with erosive bases and pebble lags (Fig. 9E), followed by parallel-laminated tabular beds in a thickening upwards sequence. These beds evolve upwards into roughly bedded or massive breccias forming the upper part of the unit. In this upper part, the breccias are arranged in a succession of inversed graded sets, separated by accretion planes dipping basinwards (Fig. 9F). Clast size increases upwards in each set from 1 to 5 cm at the bottom to blocks up to 30 cm at the top. The last set displays atop a 30–40 cm thick layer formed of subangular blocks up to 60 cm in size (Fig. 9G). This upper layer appears in all the studied sections along the outcrop, and it is directly overlain by the diapir deposit.

These facies change in thickness from 5 m (Section A) to 40 m (Section B) (Figs. 5 and 6). These lateral thickness variations are the result of the filling of a paleo-relief formed before deposition. Hence, the base of the FA-8 is interpreted as a disconformity. Finally, FA-8 is overlain by the megabreccia located at the lower interval of the diapir deposit in all the studied sections (Figs. 4, 5, and 6).

Under the microscope, the parallel laminated intervals present at FA-8 show a pervasive cement formed by macroscopic poikilotopic gypsum crystals with anhydrite inclusions similar to FA-5, FA-6 and FA-7 cements. Minor amounts of reddish clays are founded at the crystal boundaries (Fig. 8F). The alabastrine gypsum clasts are formed by microcrystalline aggregates of gypsum, surrounded by the poikilotopic cement (Fig. 8H).

4.4. The diapir deposit at the Os de Balaguer sub-basin

The lower interval of the diapir recorded at the Os the Balaguer sub-basin is formed of a megabreccia outcropping continuously along the diapir contact and overlaying the FA-8 breccias (Figs. 4, 5 and 6). This megabreccia is made of disrupted, meter sized blocks and clasts of secondary laminated gypsum and carbonates from the Muschelkalk and Keuper facies, surrounded by a fine matrix, partially cemented with sulphates. Numerous colored (reddish and black) gypsum nodules, and fibrous gypsum veins are also present within this unit (Figs. 10A, B, and C).

The megabreccia displays a general succession constituted by the alternance of two characteristic facies, packbreccias and floatbreccias, both referring to breccias lacking depositional features (Fig. 11). Floatbreccias are made of matrix-supported floating gypsum blocks, gypsum nodules, and carbonate fragments (Fig. 10C). Gypsum blocks are rounded and usually show different levels of internal deformation. Within floatbreccias, there are also meter-thick intervals defined by variations of colors and textures, as well as by the number of floating components (Fig. 10C and E). On the contrary, packbreccias are clast-supported breccias with minor amounts of matrix (Fig. 10D). Packbreccias can be formed of either laminated gypsum blocks or carbonate blocks, which can be further divided in two types of carbonate packbreccias: limestone packbreccias formed of meter-scale, M3 mudstone blocks in which sedimentary structures are still preserved but the depositional configuration is not recognizable, and dolomitic breccias with macroscopic, centimeter-sized, open porosity. Both appear intercalated within the gypsum packbreccias.

From bottom to top the succession observed in the megabreccia includes:

- Along the base of the megabreccia there is a centimeter to meter thick interval formed of folded and brecciated fibrous gypsum veins (Figs. 9G, and 11). At microscale, gypsum veins are formed of

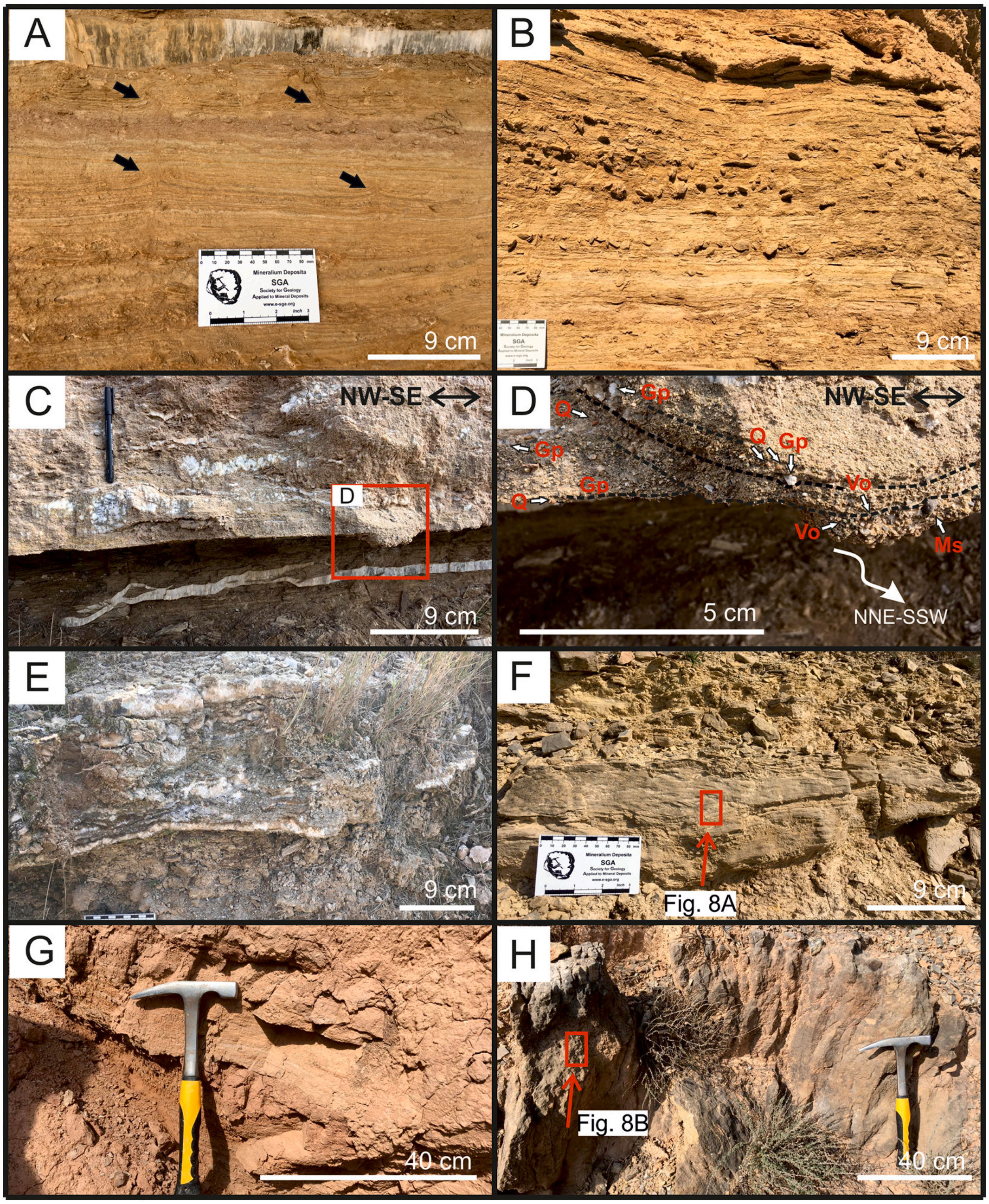

Fig. 7. A: FA-1. Laminated gypsarenites with. Black arrows point to tepee structures. B: FA-1. Laminated gypsarenites with numerous centimeter-thick gypsum lenticules and crystal aggregates. Note that they are unevenly distributed and accumulate at certain levels. C: FA-1. Base of a meter-thick microconglomerate bed with alabastrine gypsum aggregates. The base of the bed is planar and displays flute marks. D: FA-1. Small-scaled trough cross-bedded microconglomerate. The photo corresponds to the infill of the flute mark shown in C. Lithic fragments compositions are indicated (Q: quartz; Gps: gypsum clasts; Vo: subvolcanic rocks (dolerites), Ms.: M3 Muschelkalk carbonates). E: FA-2. Black lutites intercalated with centimeter-thick gypsum alabastrine beds. F: FA-3. Small-scaled trough cross-bedded arenites with intercalated marls. G: FA-4. Parallel-laminated red lutites. H: FA-4. Meter-thick tabular bed of lithic arenites. Vertical structures may correspond to root marks. This bed is intercalated between the red silts shown in G. (For interpretation of the references to colour in this figure legend, the reader is referred to the web version of this article.)

displacive fibrous crystals reflecting an antitaxial growth. Despite the deformation, the mean orientation of the veins is subparallel to the basal diapir contact. These veins engulf the blocks from the underlying upper part of the FA-8 facies (Fig. 9G).

- Floatbreccia intervals are often founded immediately over the basal veins and are predominant and thicker towards the bottom (Fig. 11). On the contrary, packbreccia intervals are thinner (1–4 m) and laterally discontinuous at the bottom, getting thicker and more predominant towards the top (Fig. 11).
- Atop of the succession there are metric to decametric, Muschelkalk (M3) carbonate, dolerite, and laminated gypsum blocks (K1–K2) (Fig. 10G). Usually, these blocks are brecciated at their base, but overall, they preserve depositional features such as lamination, bedding, or bioturbations. Nevertheless, these blocks register internal deformation in the form of fractures and folds, so the stratigraphic polarity cannot be asserted with confidence (Fig. 10H). From the top of the megabreccia the thickness of these blocks rises upwards from a few meters to tens of meters, where they also show map-scale continuity. Therefore, there is not a clear upper limit for

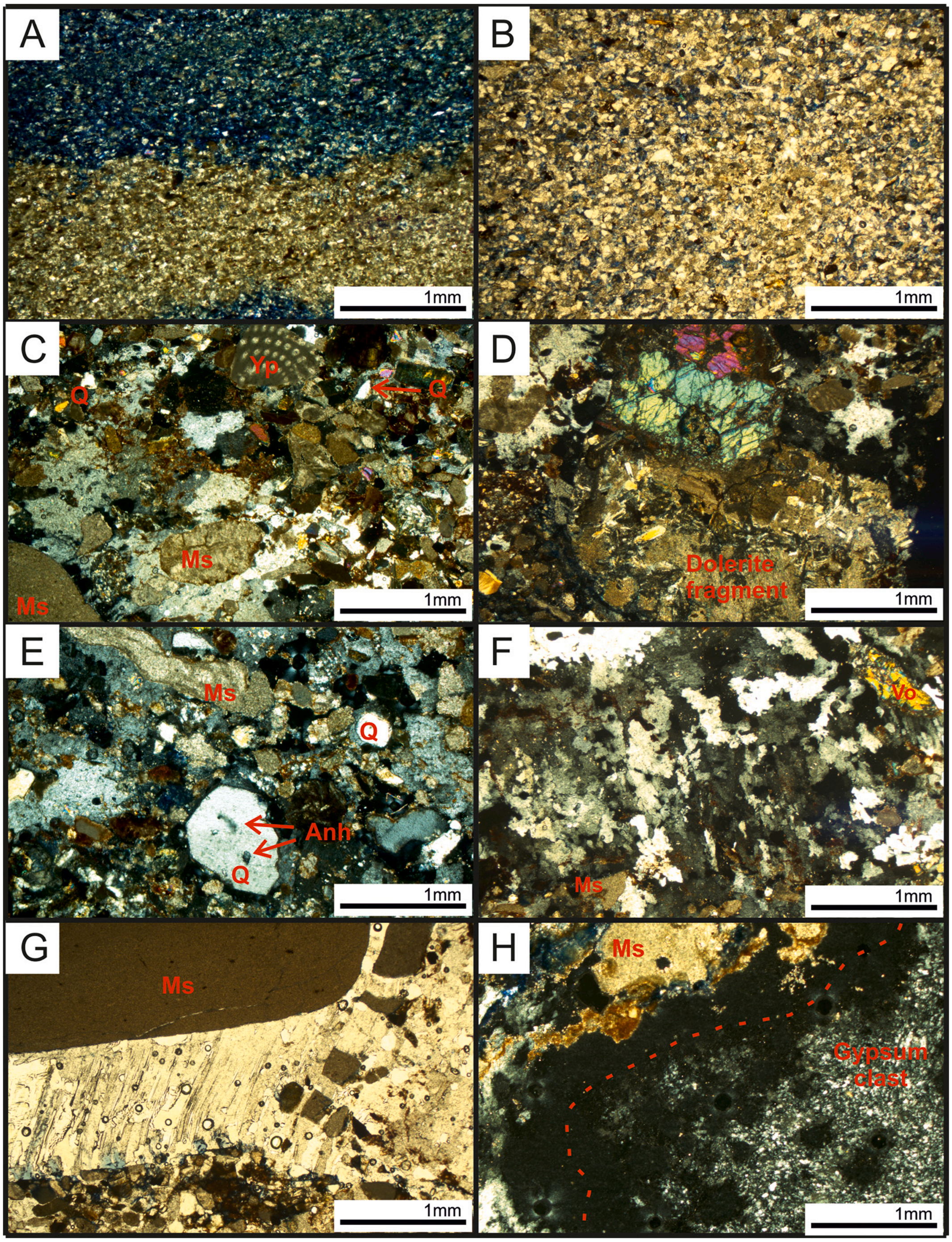

Fig. 8. Microphotographs of the main characteristics of FA-1 to Fa-8. A: Polarized light. Arenites in FA-3. Matrix rich intervals alternate with clean open interparticle porosity intervals (tinted in blue). B: Polarized light. Carbonate rock fragments and quartz grains are the main components in the FA-4 lithic arenites. C: Polarized light. Poikilotopic gypsum cement formed by large crystals with anhedral boundaries. It is observed in FA-5, FA-6, FA-7 and FA-8. D: Polarized light. Detail of a dolerite. E: Polarized light. Fragment of a quartz crystal containing anhydrite inclusions in FA-5 arenite. Inclusions suggest a diagenetic growth inside an anhydrite formation, probably the Keuper facies. F: Polarized light. Large porosity cemented with anhedral gypsum crystals. G: Plane light. Detail of a fibrous gypsum vein adjacent to a micrite clast (Muschelkalk, M3). The gypsum fibrous crystals also penetrate the fractures within the Muschelkalk clast. Secondary porosity is observed towards the lower wall of the vein. H: Polarized light. Detail of the structure of a gypsum clast. It is formed of microcrystalline gypsum crystals in the nucleus that, progressively reduce their size to a cryptocrystalline mass forming the grain boundary. (Q: quartz; Yp: Ypresian clasts; Ms.: M3 Muschelkalk carbonate clasts; Vo: subvolcanic rocks (dolerites), Anh: anhydrite inclusions). (For interpretation of the references to colour in this figure legend, the reader is referred to the web version of this article.)

the megabreccia and it instead transitionally evolves upwards into a stacked arrange of blocks that characterizes the rest of the diapir mass (Figs. 4, 5, and 11).

4.4.1. *Structural features of the diapiric megabreccia*

In floatbreccia facies, foliations and lineations are observed (Figs. 10A and 11). Rough lineations can be defined by preferred orientations in elongated floating components. This is especially noticeable in ellipsoidal gypsum nodules in which orientation is defined by the

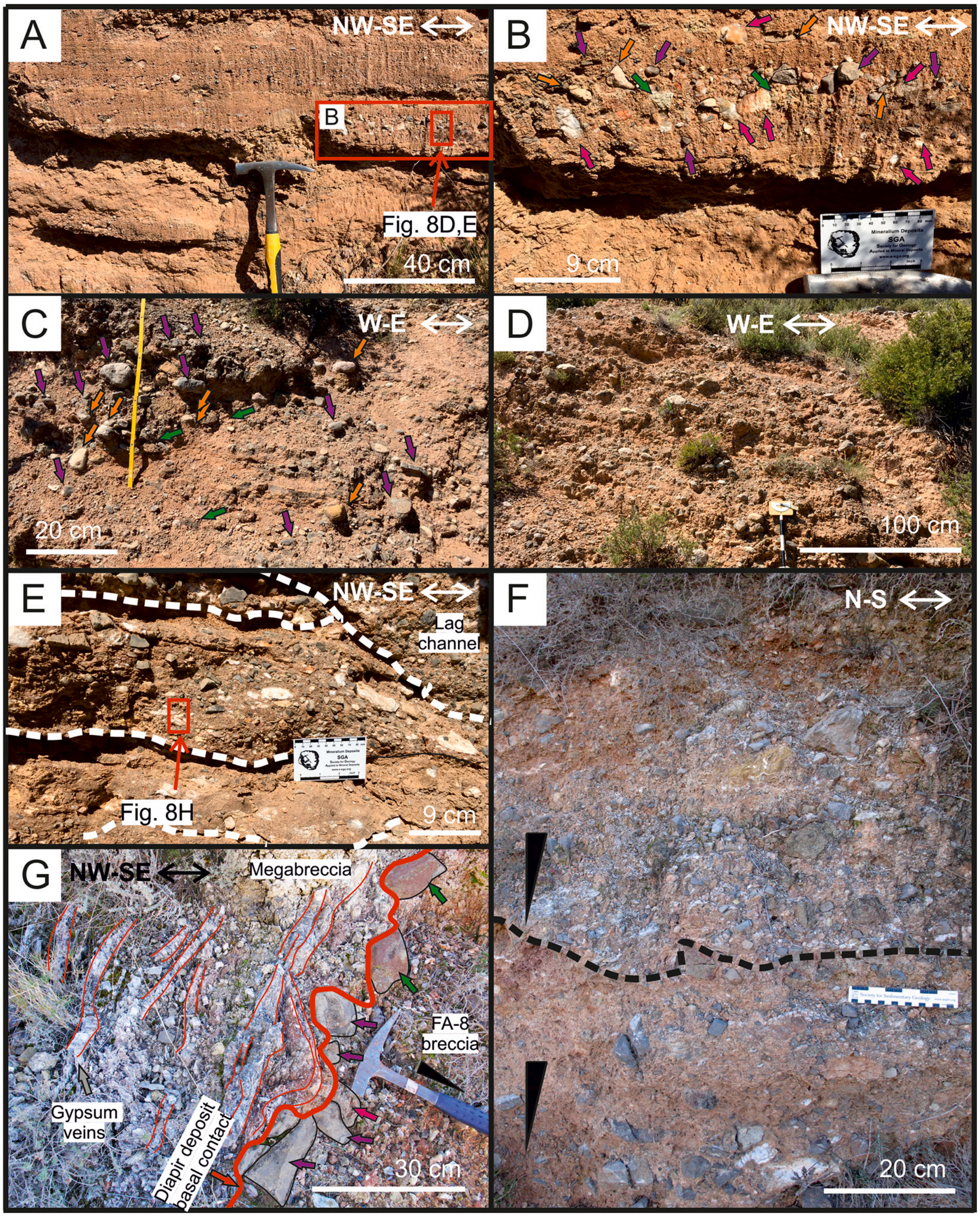

Fig. 9. A: FA-5. Planar-parallel laminated red arenite beds and conglomerates. Red lutites are intercalated between the arenite beds. B: FA-5. Detail of a basal pebble lag. Clast composition is also indicated (Gps: gypsum clasts; Vo: volcanic rocks -dolerites-, Ms.: M3 Muschelkalk carbonate fragments; Yp: Ypresian *Alveolina* Limestones). C: FA-6. Rough cross-bedded conglomerates with arenites. Clasts and blocks are floating inside a red matrix and sometimes accumulated in channel-bottom lags. D: FA-7. Rough bedded conglomerates with 20–30-cm size blocks. E: FA-8. Amalgamated channels with cross-cutting surfaces. Channel infills correspond to breccias made of carbonate fragments (Muschelkalk, M3) dolerites, and gypsum fragments. F: FA-8. Sets of inverse graded breccias with floating clast and blocks in a red matrix. Note that the base of the sets is usually erosive. Clasts size changes upwards from pebble to block up to 15–20 cm. G: FA-8. Diapir contact (marked in red). Note how the contact trace surrounds the blocks located at the uppermost level of the breccia. Above the contact, there are numerous deformed fibrous gypsum veins within a fine white matrix. (For interpretation of the references to colour in this figure legend, the reader is referred to the web version of this article.)

alignment of their long axis (Fig. 11).

In addition, the orientation of components at micro and macroscopic scales defines penetrative, relative continuous, and regular spaced planes interpreted as foliations (Figs. 10A, C and 11). Several foliations can be distinguished in the floatbreccia, arranged in subparallel, anastomosed, or folded foliations (Fig. 10A, C and F). All these foliations can coexist together in the same interval or be separated at different intervals. Foliations generally strike NNW-SSE and dip towards the NE (Fig. 4). In subparallel foliations, the general trend is subparallel to the megabreccia base. Anastomosed planes are often formed by two differently spaced families intersecting each other (Figs. 10F and 11). The more spaced family can be either sub-parallel to the megabreccia base or slightly in angle (Fig. 11). For their morphology, anastomosed foliations are probably S—C type shear-bands.

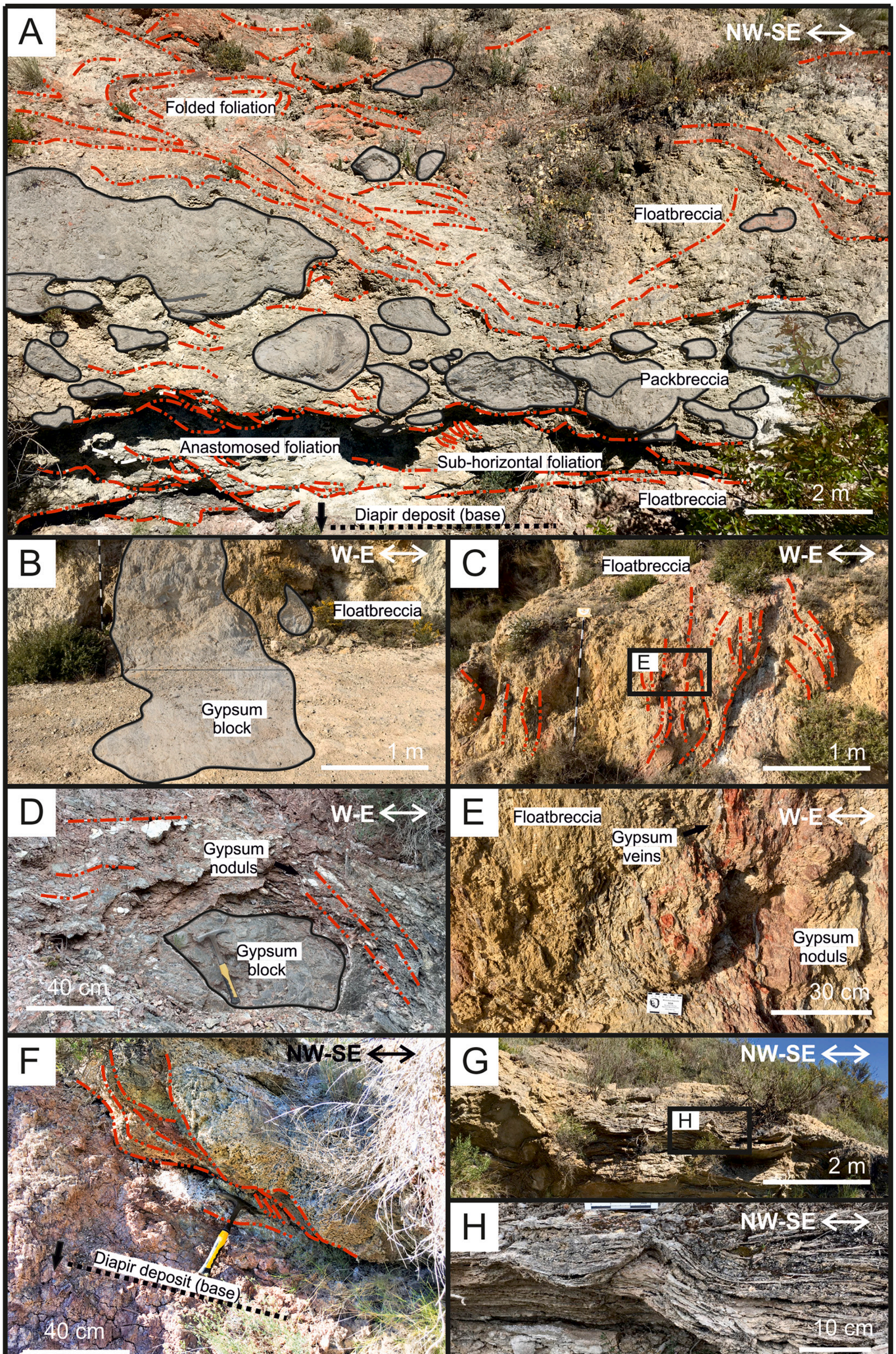

Fig. 10. A: Stratigraphic succession showing floatbreccia to packbreccia facies where different types of foliations planes can be observed. B: Isolated metric-thick laminated gypsum block within yellow lutites. C: Floatbreccia facies with vertical rough foliations concordant with aligned, red-colored gypsum nodules. D: Packbreccia facies with alabastrine gypsum nodules. Nodules are aligned according to its longest axis denoting preferential directions (lineations) marks in red. E: Floatbreccia detail. Note the presence of subvertical foliations concordant with the alignment of gypsum nodules. F: Anastomosed arranged in a similar way as S—C type planes. G: Top of the megabreccia succession showing a metric to decametric laterally continuous stringer of laminated gypsum. Although there is internal deformation (fractures and folds) in these stringers, they appear to be stacked. No floatbreccia or packbreccia facies are observed above this point in the succession. (For interpretation of the references to colour in this figure legend, the reader is referred to the web version of this article.)

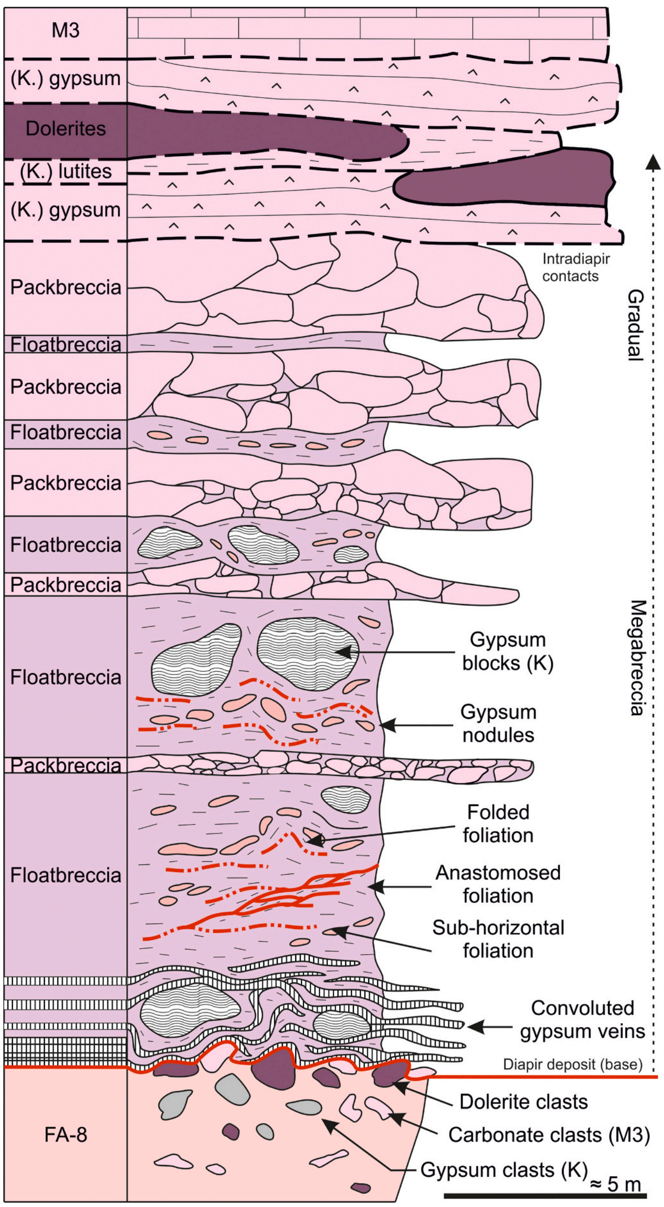

Fig. 11. Conceptual, not to scale, stratigraphic sequence of the megabreccia succession as observed along the diapir contact, and on top of the FA-8 breccia, in the Os de Balaguer sub-basin.

5. Discussion

5.1. Facies interpretations, correlations, and diagenetic constraints

FA-1 is interpreted as the deepest parts of a shallow saline lake with desiccation events (Table 1). The laminated gypsarenites were probably formed at the water surface, and then accumulated at the lake bottom as gypsum cumulates. In tune with this, the cyclical lamination (Fig. 7A and B) is probably the result of seasonal changes in water conditions which controlled the precipitation of gypsum, although the intercalated lutites were transported by aeolian processes. This kind of facies association is commonly related to relatively deep environments in coastal lakes (Warren, 1982, 2016). However, tepee structures are more typical of sabkha environments than underwater facies (Basyoni and Aref, 2015), indicating that the saline lake probably experienced events of complete desiccation. At these moments, the lenticular gypsum crystals also grew displacively inside the sediments in a phreatic environment (Aref and Mannaa, 2021). Hence, the lake was likely ephemeral, and it is suggested that water completely evaporated during arid/dry periods.

Intercalated microconglomerate and lithic arenite layers (Fig. 7C and D) represent lobes of sediment discharge towards the saline lake. Both the upwards thickening trend, as well as the increase of clastic-rich beds, reflect an increase in the occurrence and energy of these events. The presence of Muschelkalk rock fragments and dolerites (among other local carbonate fragments from the overburden sequence) indicates that the diapir was one of the source areas, which must have been already subaerially exposed and being eroded.

FA-2 represents the saline lake margins (Table 1). Lutites (Fig. 7E) are interpreted to be deposited by low energy water flows in mudflat environments (Warren, 2016). These facies represent a shallower depositional environment than FA-1.

FA-3 was deposited on the shore of a saline lake (Table 1). Small-scale trough cross-bedding, the relatively good grain sorting, highly connected interparticle porosity, and homogeneous quarzitic composition in arenites along with the absence of fine particles (Fig. 8A) are indicative of an aeolian origin. The alternation of marls and arenites (Fig. 7F) is probably the result of lacustrine currents and aeolian transport acting at different times. The grain composition indicates a mixed provenance, with external inputs, since metamorphic rock fragments are probably derived from the Axial Zone, and local inputs, mainly represented by the carbonate fragments, which are derived from the overburden units and from the diapir deposit (Fig. 8B).

FA-4 reddish laminated lutites and arenites (Fig. 7G) were deposited in distal alluvial environments (Table 1). Lutites represent overbank facies at the external parts of the alluvial system, whereas arenite beds are interpreted as amalgamated sand channels intercalated into the overbank facies. In alluvial fan systems, these facies associations are common in distal (and intermediate) parts, where channels change their position laterally over time (Blair and McPherson, 1994; Yu et al., 2018). Arenites mainly contain local fragments from the diapir and the overburden units, with some metamorphic external components.

FA-5 is interpreted as the intermediate parts of an alluvial fan system (Table 1). Planar-bedded arenites and conglomerates (Fig. 9A) represent non-channelized flows characteristic of the upper-intermediate parts of the alluvial system (Blair and McPherson, 1994). Clast composition mainly indicates a local source, from the overburden and from the diapir, although diapir-derived fragments are more numerous. Furthermore, the relatively high amount of gypsum clasts found in these facies indicates that they were deposited closer to its source area relative to the previous FAs (Fig. 9B).

FA-6 is interpreted as proximal alluvial fan facies (Table 1). Cross-bedded arenites and conglomerates have been interpreted as amalgamated channel-fill sequences lacking associated overbank facies (Fig. 9C). These deposits are next to the fan apex, where feeder channels stack and cut each other due to the limited lateral space (Blair and McPherson, 1994). Debris flow processes are the most suitable for these deposits, as they are characteristic of proximal alluvial areas (Sohn et al., 1999). The most abundant components are diapir-derived rock fragments (gypsum, Muschelkalk carbonates, and dolerites), suggesting the proximity of the extruding diapir. *Alveolina* Limestone fragments, as well as undifferentiated Mesozoic carbonate fragments, are also present indicating that the overburden units were eroded together with the diapir rocks.

FA-7 corresponds to colluvial or avalanche deposits, characteristic of the most proximal areas of an alluvial fan (Yu et al., 2018) (Table 1). The almost complete lack of depositional structures (Fig. 9D) indicates that they were formed by gravitational transport as colluvial deposits, or by highly energetic sheet/blanket flows (Davoudi et al., 2019). Muschelkalk carbonates and dolerite clasts represent the predominant fraction in the sediment composition, and therefore, these facies were settled down adjacent to the outcropping diapir.

FA-8 is interpreted as proximal alluvial deposits overlaid by colluvial deposits (Table 1). This breccia probably sedimented within a dense and energetic sheet/blanket flow capable of transporting relatively large clasts, pointing towards the intermediate to upper parts of an alluvial system (Davoudi et al., 2019). The cross-cutting surfaces with channel lags (Fig. 9E) are interpreted as rough channelized bodies amalgamated together. Debris-flow processes are the most suitable for the characteristics observed in the lower and intermediate intervals within these facies, since they show very poor sorting, floating clasts, and poorly developed internal structure (Sohn et al., 1999). In contrast, the inversed graded interval with large blocks atop is indicative of gravitational rock-fall processes (Fig. 9F). The dipping of the accretion planes observed within these gravitational deposits suggest a progradation of the system from the N-NE towards the S-SW (Fig. 4B). The inverse grading and the relatively large percentage of gypsum grains strongly suggest short transportation distances. Grain composition points to the diapir as the sole source area, since there is a total lack of local, overburden-derived inputs, and/or external inputs.

The poikilotopic gypsum cement in FA-5 to FA-8 is interpreted as a secondary gypsum due to the presence of anhydrite inclusions, sutured contacts, and the pervasive nature of the cement (Fig. 8C, D, E, F, and H). Antitaxial veins (Fig. 8G) parallel to bedding nucleated in large porous and grew after or synchronically with the poikilotopic cements. The large separation between grains within poikilotopic cements (Fig. 8F) indicates an early displacive gypsum growth before mechanical compaction. Nevertheless, these large distances between grains, together with very low matrix contents suggest the existence of detrital gypsum grains which are now missing. Anhydritization and later transformation to secondary gypsum may have erased the depositional fabric, so the pervasive gypsum cement may also have resulted from the transformation and amalgamation of detrital gypsum grains during these processes. Both types of cement are indicative of diagenetic, highly saturated, sulfate-rich fluids.

From the described FAs at the Os de Balaguer sub-basin, the sedimentary infill can be divided into two main depositional stages and a third stage characterized by salt emplacement: 1) During the first depositional stage, a saline lake located southwards and connected with a mainly north-derived alluvial system, is represented by FA-1 to FA-7. The correlation between these FAs (Fig. 12) suggests an apparent southwards progradation, also recorded by the upwards transition from distal to proximal facies, and by the southward migration of the lake system, which was finally buried by alluvial sediments. According to the measured paleocurrents (Fig. 4B), progradation direction can be further constrained as NE-SW in the northern area, and N-S direction in the southern area. These paleocurrents also suggest that the sub-basin depocenter was located at the SW, where the saline lake was initially located. 2) An important erosion with related valley incision marks the onset of the second depositional stage. The FA-8 breccia fills the paleo-relief marked by the disconformity at the base of this facies (Fig. 12). The orientation of the paleo-valleys cannot be fully deciphered from field observations, but cross-bedding at the base of the FA-8 unit suggests a NE-SW transport direction. The last stage ends with the emplacement of the diapir deposit (Figs. 4, 5, 6, and 12) over the previous sedimentary systems.

Thus, considering: 1) the overall progradation from alluvial to colluvial systems of the FA-8 (increase in transport energy); 2) the accretion surfaces observed in this facies (denoting a laterally *syn*-kinematic advancing sequence from NE towards SW); 3) the exclusive Les Avellanes diapir source area of the FA-8 components; and 4) the emplacement of the diapir deposit overlaying the previous FAs, the diapir deposit corresponds to a salt sheet which advanced from the NE towards the SW over the syn-kinematic FA-8 deposit.

5.2. Origin and deformation of the Les Avellanes diapir deposit

The diapir deposit in the Os de Balaguer sub-basin presents different facies and deformation structures. Most of the diapir deposit is formed of laterally continuous, decametric to kilometric, stacked blocks made of Muschelkalk carbonates from the M3 facies, Keuper laminated gypsum from the K1 and K2 facies, and dolerites, embedded within lutites (Calvet et al., 1994; Arnal et al., 2002; Salvany and Bastida, 2004; Camara and Flinch, 2017) (Fig. 4).

Halite or any other subordinate chlorides (salt), are not found at the surface within the Triassic in the Serres Marginals area, although their presence is confirmed in the underground by exploration wells (e.g. Lanaja, 1987), and by the existence of salt springs within the Les Avellanes diapir. The underground Triassic sequence shows salt-rich intervals, where massive salt alternates with anhydrite, carbonate, and lutite layers. Salt is mainly in the Muschelkalk facies M2, and in the Keuper facies K1 and K2, with the carbonates from the M3 interlayered between them (Camara and Flinch, 2017). Despite mineral transformations (as gypsum to anhydrite, or calcite to dolomite), the Triassic blocks forming the diapir deposit at the surface are equivalent to the

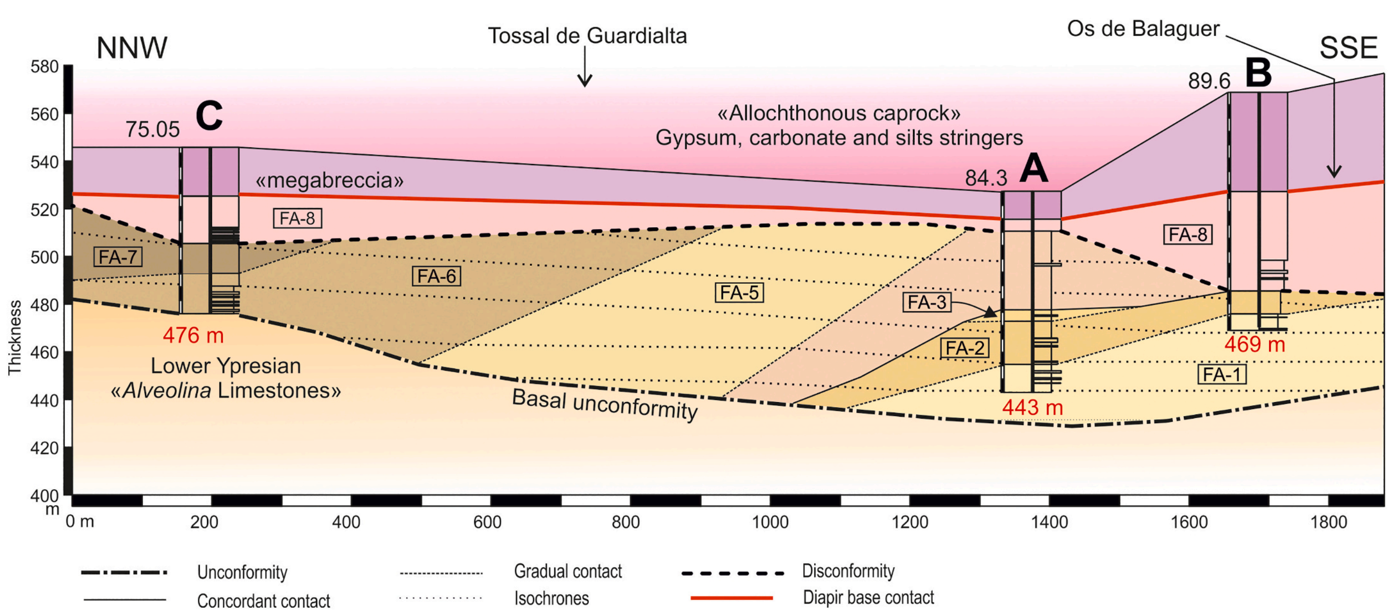

Fig. 12. Facies correlation panel along the studied area from simplified stratigraphic sections from Fig. 6. The2D correlation panel creates a representative NNW-SSE, along-strike, cross-section of the Os de Balaguer sub-basin. Real stratigraphic thicknesses are used.

intra-salt layers at depth (Arnal et al., 2002; Salvany and Bastida, 2004). Thus, the underground sequence is complete and closer to the depositional configuration.

During diapir formation, the Triassic sequence was intensely deformed as the Muschelkalk and Keuper halite-rich intervals became mobile. The competent, intra-salt layers (mainly the carbonates from the M3 facies) experienced deformation leading to their rupture by boudinage, forming pieces called stringers that were carried upwards within the salt (Rowan et al., 2019b). Since dolerites were intruding in the evaporite sequence as sills and dikes (Azambre et al., 1987), they are mechanically equivalent to the sedimentary stringers. When salt arose next to the surface, the infiltration of meteoric waters caused the dissolution of the salt and a caprock started to grow over a dissolution zone atop of the salt structure (Warren, 2006). As salt dissolved, the stringers accumulated within the caprock (Reuning et al., 2009; Thomas et al., 2015; Závada et al., 2021). Thus, the Les Avellanes diapir deposit is a caprock originating from the dissolution of the salt and the accumulation of insoluble stringers formerly entrained within salt flow (Fig. 13A).

Caprocks and carapaces (sediment accumulations atop of a moving salt sheet, typically in marine settings) are brittle crusts enveloping the mobile salt. In salt sheets and salt glaciers, the caprock is detached, and glides over the salt (Talbot and Pohjola, 2009). The brittle caprock transported over a spreading mass of salt deforms and breaks forming rafts, which drift, and usually accumulate at the front of the salt extrusion (Jackson and Hudec, 2017a). Furthermore, the deformation of the caprock deposit can be modelized to infer the direction of salt flow (e.g., Sarkarinejad et al., 2018). The arrangement of stringers within the caprock often resembles a recumbent fold and thrust system, where stringers are imbricated pointing towards the direction of advance (Rowan et al., 2020a). In addition, mylonitic fabrics (foliated gypsum) can also be related with salt flow as the caprock registers shear strain during the movement of the salt (Závada et al., 2021). In this sense, the alignment of gypsum components within salt structures has been attributed to syn-kinematic, solution-precipitation creep processes, analogous to porphyroblasts in a metamorphic fabric (De Meer et al., 1997; Závada et al., 2015). The stacked stringers within the Les Avellanes caprock deposit in the study area, are mainly imbricated, dipping towards the NE (Fig. 4B), and its arrangement resembles the expected direction of advance (from NE to SW) in this area. In addition, the foliation recorded within the basal megabreccia is subparallel to the arrangement of the stringers, and to the contact between the caprock deposit and the sedimentary units, also registering the caprock movement atop of a salt. However, tectonic shortening can produce similar deformation in caprock deposits and overwrite the structures related with salt flow. Thus, linking the caprock deformation solely to salt flow is challenging (Závada et al., 2021). Nevertheless, since deformation is not present in the sedimentary facies below the megabreccia, the contact between the caprock megabreccia and the FA-8 (Fig. 9G) cannot be interpreted as a fault. Instead, the caprock was detached over a layer of flowing salt and carried on as gliding rafts on top of a salt sheet which advanced over the sedimentary facies below (Fig. 13B).

With regard to the nature and emplacement of the megabreccia at the lower part of the caprock, two origins are considered according to the position of the salt layer, which in turn influences the position of the deformation associated with the advance of the salt sheet. Considering that the salt was located directly above of the FA-8 sedimentary facies, the megabreccia was probably formed as a dissolution breccia (Fig. 13C). As salt dissolved at the front of the extrusion, the lower part of the caprock in contact with the salt collapsed, forming the megabreccia deposit. The shear deformation is recorded during the megabreccia formation, as the remaining salt in the inner part of the extrusion

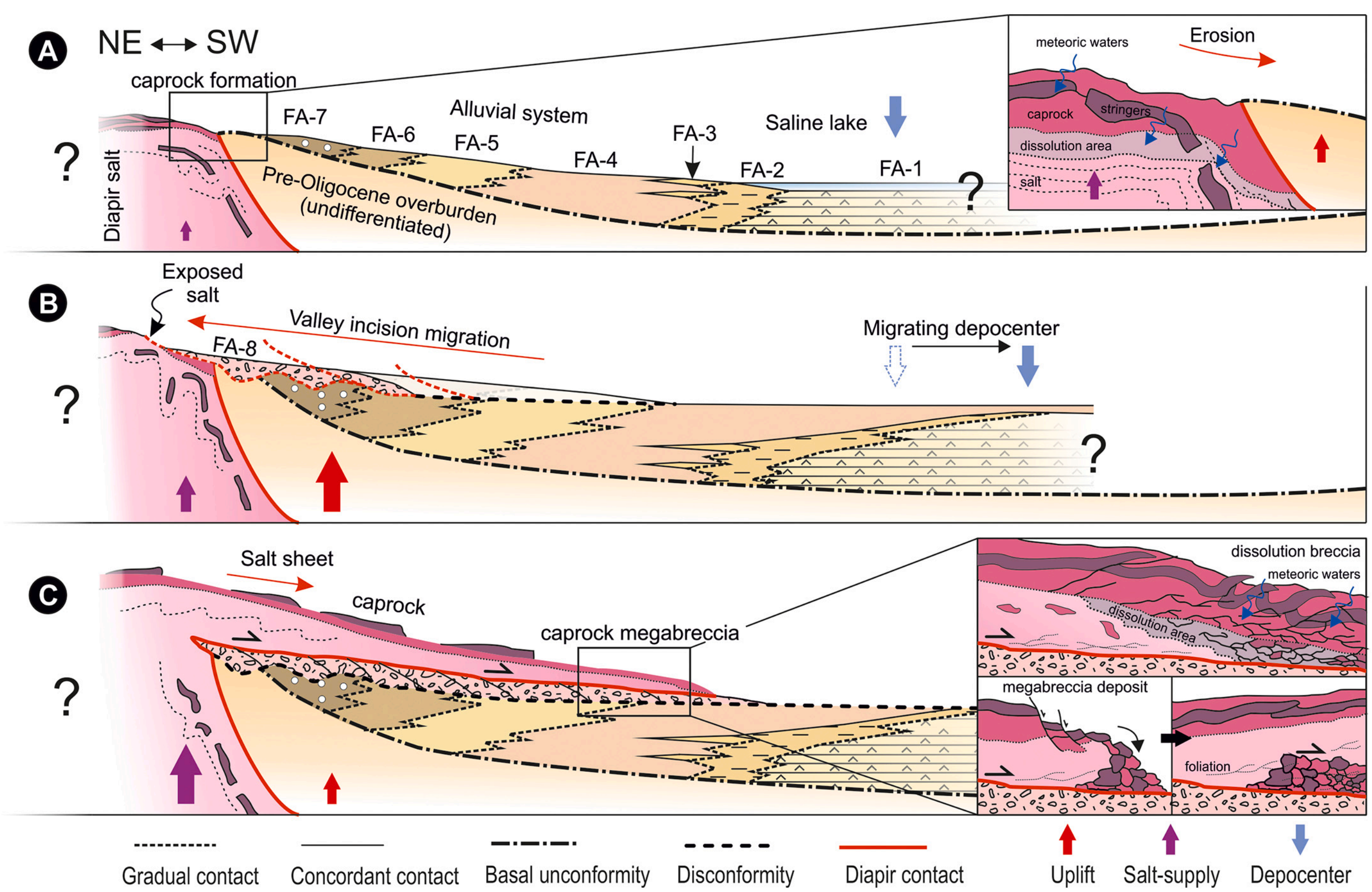

Fig. 13. Not-to-scale conceptual model showing the processes controlling the sedimentary evolution and salt sheet emplacement in the Os de Balaguer sub-basin.

is still advancing and exerting pressure towards the front. This origin is supported by the upward gradual succession from floatbreccia to packbreccia facies (Fig. 11), and the presence of a dense belt of antitaxial gypsum veins along the contact between the FA-8 and the megabreccia (Fig. 9 G). Gypsum crystals in the veins probably started to grow inside the porosity created by the dissolution of the salt and the collapse of the stringers atop of it. The megabreccia can also be a deposit made of brecciated stringers, overrode by the salt sheet (Fig. 13C). As caprock rafts reached the frontal areas, they became brecciated forming a deposit made of blocks that was settled along the front of the salt sheet. Then, as salt extrusion continued, this deposit was overridden by the salt and emplaced underneath the salt sheet. Shear deformation within the megabreccia was caused by the salt advancing on top of it. Then, when all the salt was dissolved, the rest of the caprock was settled over the megabreccia. In this case, some intrasalt debris left after salt dissolution should be recorded atop of the megabreccia, but they are not observed in the studied profile.

With regard to of salt sheet emplacement there is an ongoing debate over the nature and location of deformation. On one hand, numerical modeling has predicted the existence of *syn*-kinematic deformation in the rocks beneath a salt sheet, called “shear zones” (e.g., Alsop et al., 2000; Hudec and Jackson, 2009; Nikolinakou et al., 2019). According to these models, shear zones are formed by the advance of a salt sheet over non-consolidated sediments at its front, which tend to form nappe folds overthrusted by the salt while advancing. High pore pressure within the frontal sediments facilitates deformation below the salt sheet (Nikolinakou et al., 2019). On the other hand, exploration wells often find, a highly deformed, and usually brecciated interval, named “rubble zone” directly under the salt sheet (Saleh et al., 2013). These have been interpreted as slumped carapaces deposited in front of the salt sheet over the sea floor, and subsequently overridden by salt advance (Jackson and Hudec, 2017b). Observations in surface analogs show a different relation (Hearon IV et al., 2015; Rowan et al., 2019a; Rowan et al., 2020b) and instead there is usually no clear deformation beneath allochthonous salt structures. In tune with these hypotheses, in the Os de Balaguer sub-basin, there is no evidence of syn-kinematic deformation in the sedimentary sequence below the salt sheet deposit. However, as salt is not recorded, the location of deformation in relation with the salt cannot be completely asserted. If the megabreccia is considered as a sediment overrode by the salt sheet and emplaced under the salt, shear deformation caused by the advancing salt on top of it propagated below the salt sheet. If the megabreccia is considered as a dissolution breccia, the caprock glided atop of the salt layer and the deformation relative to the advance of the salt sheet did not propagate below its base.

5.3. Emplacement of the Les Avellanes diapir in the Os de Balaguer sub-basin

The comprehensive study of the Os de Balaguer sub-basin infill suggests a sedimentary system controlled by the Pyrenean evolution and the development of the Les Avellanes diapir.

In this sense, during the first depositional stage, there is a prevalence of Muschelkalk carbonate and dolerite rock fragments together with detrital gypsum clasts, being dominant upwards during the second depositional stage. These clasts indicate a relative uplift of the pre-Oligocene sequence, its erosion, and the onset of the diapir extrusion. Combined with the observed sedimentary criteria (paleocurrents, progradation, and accretion directions, as well as the distribution of the proximal and distal facies), the diapir extrusion was most probably located in the north or northeastern part of the studied area (Figs. 13 and 14). The evolution of the diapir can be divided into 3 stages according to the stratigraphic and petrographic analyses:

Stage 1: As pointed out in the previous section, initially a saline lake developed near the depocenter of the Os de Balaguer sub-basin, close to the emerging syncline fold axis (Figs. 13A, 14A.1 and B.1). The sub-basin was progressively filled and buried by the alluvial deposits coming from the northeast, where the area was being uplifted (Figs. 13A, 14A.2 and B.2). This high area was probably formed by the development of contractional structures linked with the southwards displacement of the South-Central Pyrenean thrust sheets during the early Oligocene in the study area (Grool et al., 2018; Cruset et al., 2020). The development of salt-cored detached folds weakened the overburden near the hinge, favoring the piercing, and then the extrusion of the salt (Fig. 14A.2 and B.2). When salt extruded at the surface, salt dissolution occurred, first probably by the infiltration of meteoric fluids and then during sub-aerial exposure, causing the formation of a caprock, where the rigid and non-soluble stringers accumulated. The erosion, transport, and sedimentation of the caprock deposit together with the uplifted overburden are recorded in all the detrital facies, since clasts were transported southwards by the local alluvial systems and settled in the adjacent Os de Balaguer sub-basin (Fig. 13A). Due to the probable, almost restricted nature of the sub-basin, most of the quartz grains are probably re-sedimented from the erosion of the overburden (from the Adraén formation, the Calcària de les Serres formation, and/or the *Alveolina* Limestones). Quartz fragments containing anhydrite inclusions are also probably derived from authigenic quartz crystals which grew within the Keuper facies in the underground and were inside the caprock. However, other quartz grains and metamorphic clasts, mostly present in FA-3 and FA-4 associations, indicate a minor external input to the sub-basin through the main *E*-W drainage systems developed during the early Oligocene (Garcés et al., 2020) (Fig. 14A.1).

Stage 2: As deformation progressed and salt was raising towards the surface, the northern area elevation increased, favoring the incision of the valleys. The headward incision reached the area where the salt extruded and further excavated the caprock on top of the salt until the salt below was exposed (Figs. 13B, 14A.3 and B.3). The erosion exerted by these incisions triggered a lateral salt extrusion, and the paleovalleys acted as preferred outflowing paths, allowing the salt below the caprock to advance southwards as an extrusive salt sheet (Fig. 14A.3). The caprock was then dismembered and transported as rafts above the salt. The base of the caprock collapsed as salt was being dissolved underneath during the motion of the salt sheet, also registering shear deformation. The sediments solely derived from the erosion of the caprock, were then deposited very close to the salt sheet as alluvial/colluvial deposits (FA-8) which initially filled the paleovalleys with no record of external inputs (Figs. 13B, 14A.3 and B.3). The caprock rafts arriving to the front of the salt sheet could formed a deposit made of disrupted stringers, which then was also overrode by the salt sheet.

Stage 3: As the salt extruded at a greater rate than the sedimentation rate of the *syn*-kinematic sediments (FA-8), the salt sheet overrode these facies (Figs. 13C, 14A.4 and B.4). The accretion direction of the FA-8 breccias suggests that the advance of the salt sheet was towards the S or SW, which may also be favored by the regional north to south slope of the orogenic wedge. Its advance westwards was probably prevented by the highs formed by the Os de Balaguer syncline limbs (Fig. 14A.3). Nevertheless, since no similar *syn*-kinematic rocks are preserved southwards, the total area covered by the allochthonous salt cannot be asserted with confidence.

The collected data do not allow us to fully assert whether the salt extruded through one or multiple feeders in the study area, and to discriminate between the existence of a salt sheet or a salt canopy. Different salt sheets amalgamated together are usually recorded by intense deformation zones and debris in between (Jackson and Hudec, 2017a). In this regard, the megabreccia along the base of the caprock can also be interpreted as an ablation breccia (Warren, 2006), which was left by a previous salt extrusion and then overrode by a second extrusion event. Since the contact between the megabreccia and the rest of the caprock is gradual, without presenting intense deformation or debris concentrated on top of the megabreccia, the salt extrusion probably occurred as a single event.

Considering the Os de Balaguer lateral extrusion as a single event and that during the early Oligocene the shortening in the external thrust

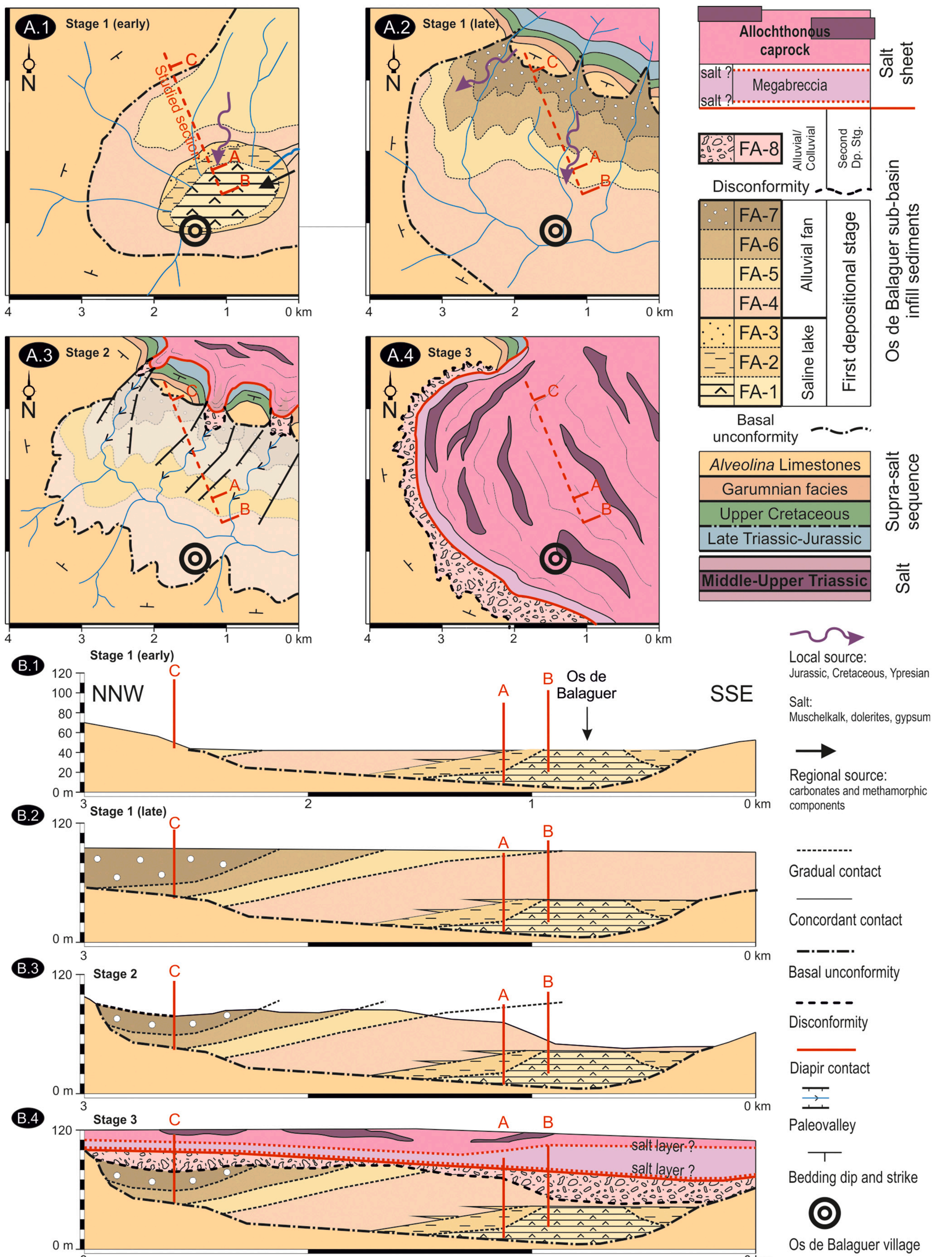

(caption on next page)

Fig. 14. Paleogeographic and depositional model of the Os de Balaguer sub-basin in relation to the Les Avellanes diapir. Stages 1, 2, and 3 are derived from stratigraphic relationships. A: map view of the inferred paleogeography. B: cross-section panels. The legend is arranged summarizing the stratigraphic relations and main events interpreted in this work. Stage 1, A.1 and B.1. Local (N-S) and external (*E*-W) derived clastic inputs arrived at a saline lake located at the depocenter of the sub-basin. Stage 1, A.1 and B.1. Local (N-S) and external (E-W) clasts are transported towards a saline lake located at the depocenter of the sub-basin. Stage 1, A.2 and B.2 the piercing of the salt at the NE of the sub-basin is recorded by a prograding alluvial system which buried the saline lake. Stage 2, A.3 and B.3. The uplift of the NE area caused the incision of the drainage network in this area. The headward erosion triggered the lateral extrusion of the salt, which flowed downslope following the pathways formed by the paleovalleys. The erosion of the caprock produced the accumulation of syn-kinematic breccias (FA-8) which then were overrode by the salt. Stage 3, A.4 and B.4. The salt sheet covered the sedimentary facies deposited in the Os de Balaguer sub-basin. The caprock was transported as rafts gliding on top of the salt.

sheets was probably greater (Beaumont et al., 2000; Garcés et al., 2020), the accumulation and piercing of the salt was controlled by the development of contractional structures, although the precise mechanisms are uncertain. To uncover these processes a more regional study is necessary, which is beyond the scope of this paper.

5.4. Salt sheet advance model

The presented data can also be used to infer a qualitative conceptual model to assert how the movement of an extrusive salt sheet can be recorded by the adjacent *syn*-kinematic stratigraphic architecture in continental settings. In this sense, salt movement can be modeled from the interplay between the four final controlling parameters: salt supply (also controlled by the tectonic shortening and/or extension rate), sedimentation rate, erosion rate, and salt (chlorides) dissolution. However, the shape of the salt structure can also be modified by local and regional deformation. These are not represented here since can vary significantly from different geological settings and ages (McGuinness and Hossack, 1993; Koyi, 1998; Peel et al., 2020). In this work, we also account for the topography of the area adjacent to the extruding salt as a controlling parameter for salt displacement. The aim is to build a logical framework, employing the stratigraphy of the sedimentary sequence deposited under or adjacent to the salt sheet, as a proxy to infer the relative salt movement.

Based on current salt glaciers (Talbot and Aftabi, 2004; Talbot and Pohjola, 2009), is assumed that an extrusive salt sheet mass behaves as a viscous fluid (Jackson and Hudec, 2017a). Therefore, in a simplistic approximation, a salt sheet is an extrusive fluid mass that moves laterally over a perfectly flat surface (Fig. 15). To quantify the salt sheet advance, the distance between the feeder and the salt front is measured in a 2D cross-section, being the reference point the feeder wall contact. This distance can change over time since the salt sheet can advance, which results in an increasing length, or can be eroded, which results in a decreasing length. Thus, the advance of a salt sheet is ultimately controlled by the interplay between salt supply and erosion rates. The salt supply rate describes the amount of salt expelled from the feeder. If erosion is not considered, an increasing salt supply rate means a progressive advance of the salt sheet (Fig. 15A). If erosion is then

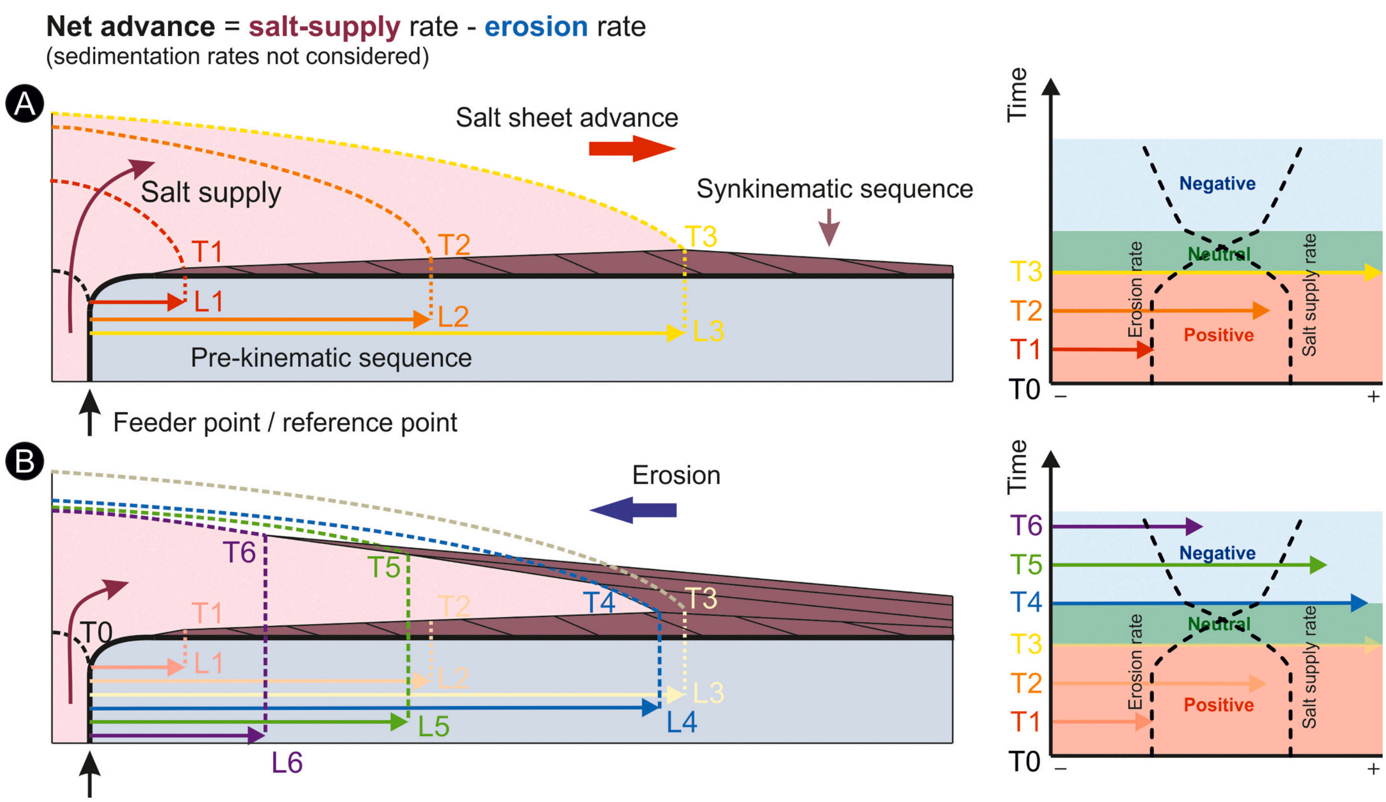

Fig. 15. Representation of a 2-D cross-section (not-to-scale) of an extrusive lateral advancing salt sheet. T1 to T6 represent consecutive time steps. L1 to L6 is the maximum horizonal length of the salt sheet measured from the feeder point to the salt sheet front at each corresponding time step. If salt supply is greater than the erosion rate, the salt front will advance laterally (A). If, on the contrary, the erosion is greater than the salt supply rate, the salt front will recede (B), and the length of the salt sheet will decrease over time. The relationship between the salt supply rate and the erosion rate is named "Net advance". When during two or more consecutive time steps the length of the salt sheet increases, the net advance has a positive value, whereas if the length decreases, the net advance is negative. If there are no significant changes on the length of the salt sheet the net advance is neutral. Syn-kinematic sedimentation has only been drawn as reference without considering sedimentation rates.

considered, an apparent retreat of the salt front by the evacuation of material out of the system is expected (Fig. 15B).

The salt supply rate depends on the intensity of the forces responsible for salt flow (such as sedimentary loading or tectonic forces) (Koyi, 1998; Hudec and Jackson, 2007). The available salt is limited because the migration of the salt feeding the lateral extrusion is eventually terminated, either by welding, or by the ceasing of the forces which originated the extrusion. This process is considered independently of later reactivations, which can again initiate the salt sheet motion. Even if the system is mainly governed by sedimentary loading, the salt extrusion is terminated once the source layer is depleted or the channel welded (Hudec and Jackson, 2006, 2007) so, considering a lateral salt extrusion, the salt supply rate follows a decreasing trend over time (Fig. 15). The erosion rate is mostly controlled by external factors such as the overall geological setting, the local topography, and the climate (mainly in onshore settings) but also by local factors such as the available salt at the surface. In this sense, when the diapir is mainly controlled by vertical movements, the area covered by the salt is minimal (Alsop et al., 2016). When, the extrusion progresses, the available amount of salt to be eroded increases progressively because the total area has also increased. While the external factors controlling the erosion can be constant, the spreading of salt over time leads to the rising of the erosion rate locally. Thus, as the salt supply decreases, the erosion rate increases, so the salt advance slows down over time, then stagnates, and finally recedes (Fig. 15).

The apparent displacement of the salt sheet can be referred as the "net advance" considering the amount of advancing salt, minus the amount of eroded material (Fig. 15). Without considering other parameters (such as external factors like climate imprint), the net advance is initially positive as the salt supply rate surpasses the erosion rate, and then tends to be negative when the erosion rate is greater than the salt supply rate. Nevertheless, the topography (simplified as the slope on which the salt sheet is advancing), the amount of sedimentation adjacent to the salt sheet, and/or the intensity of salt dissolution, are parameters that control this system (McGuinness and Hossack, 1993; Peel et al., 2020). These parameters are discussed below:

5.4.1. *Topography*

Salt glaciers flow downslope covering low areas and surrounding topography highs (Jackson and Hudec, 2017a). Considering a fixed and constant salt supply rate, the displacement of the salt is favored if salt advances downhill, thus registering a positive net advance (Fig. 16A.1), and hindered uphill, thus registering even a negative or neutral net advance (Fig. 16A.2).

5.4.2. *Syn-kinematic sedimentation adjacent to the salt sheet*

Sediments deposited adjacent to a salt sheet can be derived from both the diapir itself, its overburden and/or external sources. The accumulation of these sediments is only possible when there is enough accommodation space available during salt sheet movement. Locally, the erosion of the salt deposit is the main process controlling the amount of sediment available, and can cause both, the retreat of the salt sheet front, and the rise of the local sedimentation rate. Thus, the relationship between the sedimentation rate and the salt supply rate conditions the salt sheet shape (McGuinness and Hossack, 1993). If the sedimentation rate is low and the salt supply rate is high, the salt sheet climbs through the stratigraphic sequence as the subsalt strata pinch out towards the basal salt-sediment contact (Fig. 16B.1). If the sedimentation rate is close to the net salt supply rate or higher, the advance can be inhibited, and the salt-sediment contact is vertical or the strata onlaps the salt roof (Fig. 16B.2) (Jackson and Hudec, 2017a).

5.4.3. *Salt dissolution and caprock thickening*

The uneven distribution of the caprock along a salt sheet produces a remarkable difference in rheology, brittle in the upper and external parts where the caprock is thicker, and ductile in the lower and inner parts,

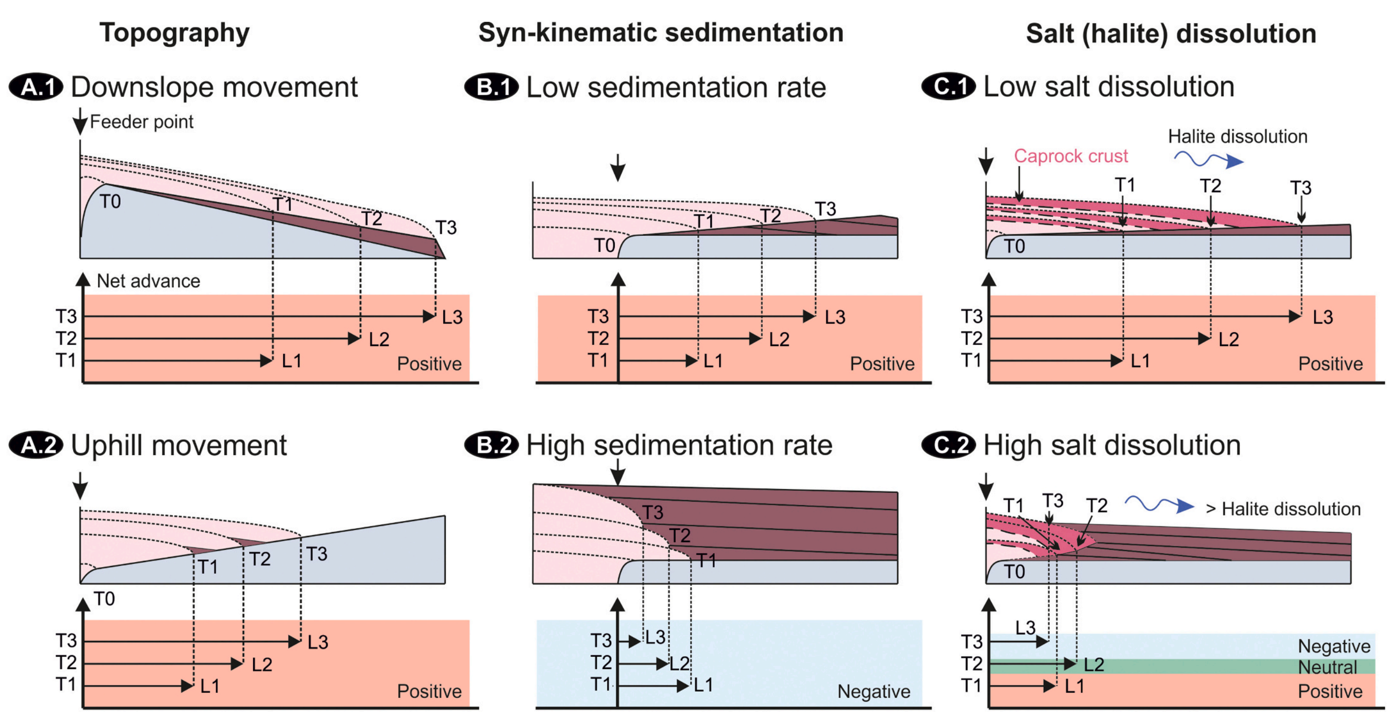

Fig. 16. Ideal conceptual model (not-to-scale) of the expected behavior of an extrusive lateral advancing salt sheet in terms of (A) the topography of the adjacent area, (B) the sedimentation rate of the syn-kinematic sequence accumulated adjacent to the salt sheet front, and (C) the amount of salt loss through dissolution and subsequent caprock growth. A.1 the salt sheet is moving downslope, so the net advance is positive. A.2 the salt sheet is moving uphill so the net advance evolves from positive to negative. B.1 In the case of a low sedimentation rate the net advance remains positive. B.2 in the case of a high sedimentation rate, the advance is hindered and the strata onlap and overlay the salt roof. C.1 If salt dissolution maintains a low rate over time, the subsequent caprock growth is low, so the salt sheet maintains its advance. C.2 If salt dissolution is high, the caprock grows at a higher rate, so the lateral movement of the salt sheet decreases or stops.

where salt is protected. The rupture of the caprock during salt sheet movement (Rowan et al., 2020a) repetitively exposes the salt enhancing its dissolution in an overall, continuous process. Therefore, the caprock is expected to extend and thicken until there is no significant salt content within the salt sheet. Hence, if the dissolution of the salt is enough or complete, the movement can be obstructed or prevented.

In actual salt glaciers, the alteration of the deposit by salt dissolution is well observed along radial or linear core-to-front cross-sections (Talbot, 1998; Závada et al., 2021). At the feeder area where salt arises to the surface, the amount of salt within the deposit is significantly greater than in the frontal parts. The progressive reduction in salt outwards is interpreted as the ongoing alteration of the salt sheet mass while advancing, and thus, at the frontal parts the salt is almost nonexistent (Warren, 2006). Most of the studied salt glaciers show a belt of folds and thrusts within the caprock at their advancing front, which can be mechanically explained as produced by local shortening as the pressure exerted by the extruding salt propagate towards the front (Závada et al., 2021).

The grade of alteration of the salt sheet in continental settings may also depends on climate conditions (Warren, 2006). In arid conditions, weathering is low, so the salt sheet movement is higher (Fig. 16C.1). Contrarily, in wet climates, the relative high weathering enhances salt dissolution so the caprock can form very early, even hindering the salt movement from the beginning (Fig. 16C.2). Nevertheless, even in the desert of Iran, the salt glaciers are altered (Závada et al., 2021). Through enough time, a caprock is formed preferably at the front of the salt sheet, hindering its advance.

5.4.4. *Relation between salt sheet movement and sedimentation*

As the net advance of the salt sheet is recorded by the *syn*-kinematic sequence deposited in the salt sheet front, the apparent displacement of the salt sheet can be deciphered from the study of the syn-kinematic stratigraphic sequence in terms of progradation, aggradation, or retrogradation. In this sense, if the net advance is positive, the salt front moves forward and the stratigraphic sequence registers the progradation of the proximal facies over the distal facies, and the salt finally overrides the sedimentary units in front of it (Fig. 17A). In this case, the base of the salt sheet dips towards the feeder. If the net advance is neutral, the salt sheet front remains approximately at the same position, so the stratigraphic sequence registers aggradation and the salt sheet contact is subvertical in cross-section (Fig. 17A). On the contrary, if the net advance is negative, the adjacent strata onlaps the salt surface and the stratigraphic sequence registers retrogradation (Fig. 17A). In this case, the top of the salt sheet contact dips basinwards.

Variations of this stratigraphic sequence are caused by the described parameters that can obstruct salt flow. In Fig. 17(B.1 to B.8) 8 different possibilities combining these parameters are represented.

There are two end-members regarding the net advance: 1) When salt is moving downhill, the sedimentation rate is low and the dissolution of salt is minimal, it is expected that the stratigraphic sequence only registers progradation and the salt sheet covers large areas in a short time period (Fig. 17B.1); and, 2); on the other hand, when it moves is uphill, the sedimentation rate is high, and salt dissolution is intense, salt extrusion may not take place and the facies will rapidly aggrade and then retrograde burying the salt sheet (Fig. 17B.8). Intermediate situations can be obtained when the three parameters act combined, enhancing and preventing the salt sheet advance, a fact that will be reflected in the syn-kinematic sequence as progradation, aggradation or retrogradation architectures (Fig. 17B.2 to B.7). The prevalence of these stages can change depending on the specific conditions under which the salt movement takes place. If the net advance is positive during a long period, the area covered by the allochthonous salt can be relatively important and the advance can be quick. If the neutral or negative stages predominate, the salt sheet movement is slow, and the area covered is smaller.

Combining the mentioned parameters and the geometry of the Os de Balaguer salt sheet (Figs. 13 and 14) is possible to approximate the area and the relative timing of the extrusion to present this salt sheet as a case-of-study.

The Os de Balaguer salt sheet advanced downhill favored by the topographic slope that is inferred by the direction of the paleovalleys and the deposition of the alluvial system. The salt sheet was emplaced over the syn-kinematic breccias FA-8, pointing that the sedimentation rate was lower than the salt supply/erosion rates. The salt sheet deposit is characterized by an extensive caprock carried atop the salt, and its formation during the lateral extrusion may have prevented its further advance. The stratigraphic architecture displays a progradation of the proximal facies over the distal ones and the geometry of the diapir deposit is irregular, although the salt sheet climbed over the sedimentary facies below.

In conclusion, there are two possibilities for the Os de Balaguer sub-basin deposit: (Fig. 17, B.1 and B.2). Thus, the projected area covered by the allochthonous salt was probably extensive in relation with the piercing area, and the emplacement of the salt sheet was quick, during a single event.

6. Conclusions

The stratigraphic record in the Os de Balaguer sub-basin is controlled by the evolution of the Les Avellanes diapir. Thus, the complete sedimentary sequence is directly related to the erosion of the Les Avellanes diapir during ongoing orogenic deformation, from its initial piercing and surface extrusion to its lateral emplacement as an allochthonous salt sheet.

The Os de Balaguer sub-basin sedimentary infill has been divided into 8 different facies associations arranged in two depositional stages separated by a disconformity. The first depositional stage (FA-1 to FA-7) includes two connected depositional systems: 1) a saline lake recorded by a succession of fine laminated gypsarenites, lutites, and gypsum beds with arenites on top, interlayered with local-derived, coarse arenites and microconglomerates; and 2) a complete alluvial succession from distal to proximal facies transporting mainly diapir-derived fragments, including detrital gypsum clasts. The second depositional stage is deposited over an important erosion and valley incision over the sedimentary succession. This paleo-relief is filled by syn-kinematic, alluvial-to-colluvial breccias (FA-8), resulting from the erosion of an extruding allochthonous salt sheet. These breccias were sedimented at the front of the advancing salt sheet and then were overrode. The salt sheet finally overlayed all the previous deposits and covered the sub-basin.

The facies, stratigraphic architecture, paleocurrents and sediment composition are used to decipher a north-eastern uplifted area with Triassic evaporites cropping out. Salt dissolution occurred at the surface where a caprock, characterized by the accumulation of stringers carried upward within the salt, started to form. The uplift and the NE-SW progradation of the sedimentary system is linked in the study area with the Pyrenean compression during Oligocene times. The progressive uplift of the northern area favored the progressive valley incision northwards by headward erosion that finally reached the extruding salt. This process opened preferred outflowing paths for the salt, and triggered a gravity driven lateral salt extrusion, which moved southwards favored by the topographic slope. The salt advanced as an extrusive salt sheet carrying rafts of caprock gliding on top and was emplaced over the sedimentary rocks. The megabreccia present along the salt sheet base, above the FA-8 facies, recorded shear deformation linked with the advancing salt sheet. This megabreccia can either be a dissolution breccia, formed by dissolution of salt below the detached caprock during the extrusion, or a deposit formed by the accumulation of intensely deformed caprock rafts at the front of the salt sheet, subsequently overrode by the salt.

Taking into account the evidence presented regarding the advance and emplacement of a salt sheet at the Les Avellanes diapir area, we can also conclude that: 1) the map trace of the outcropping diapir deposit, previously defined as a diapir contact, cannot be entirely related to a

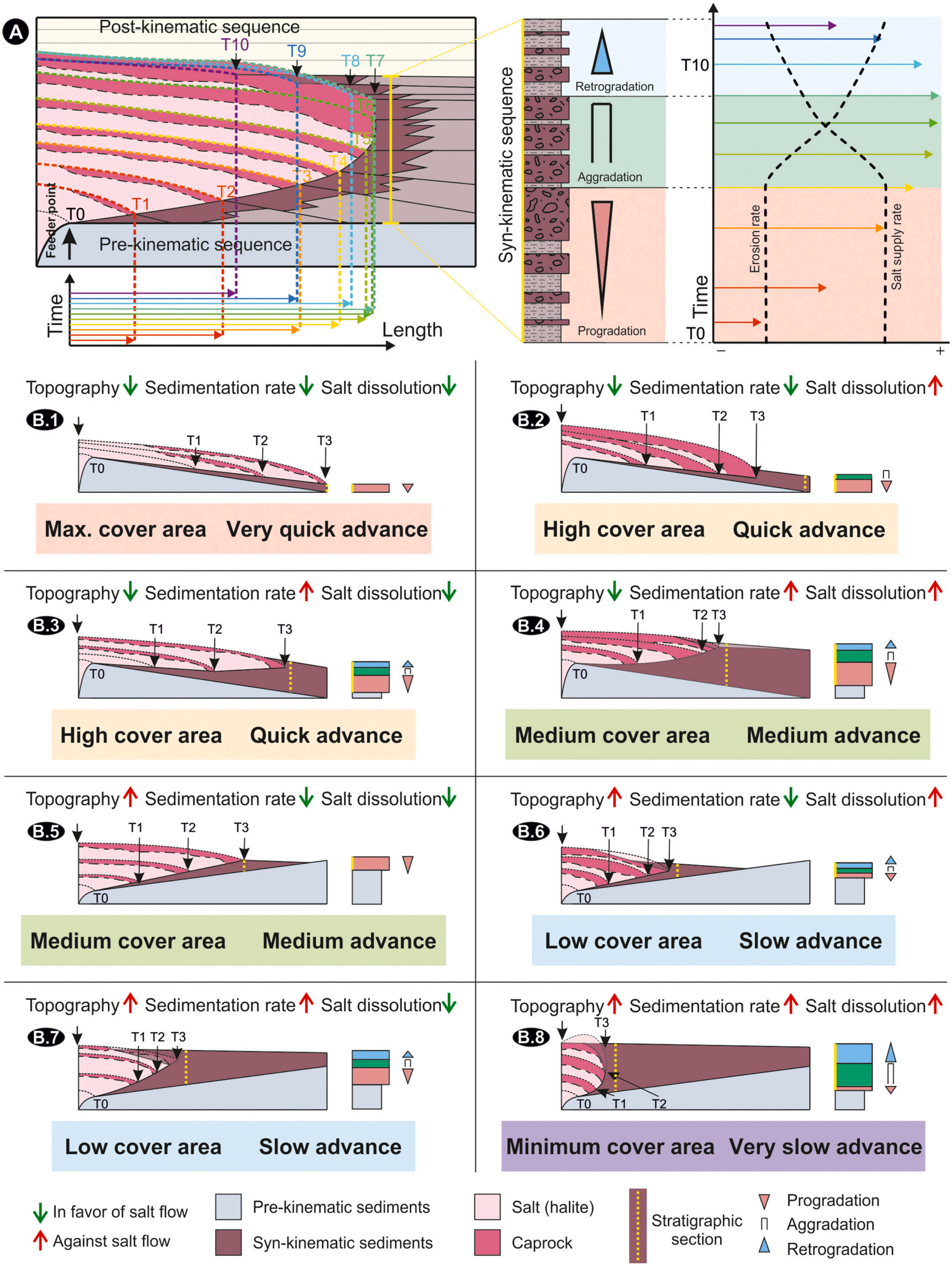

(caption on next page)

Fig. 17. Theoretical 2D diagrams (not-to-scale) of stratigraphic architecture and salt sheet emplacement versus topography, sedimentation rate and salt dissolution A: Idealization of the sequence of emplacement of a salt sheet in a core-to-front cross-section where each colored line represents a different moment in time (T1 to T10). The net advance is measured by the length of the salt sheet for each time. The emplacement of the salt sheet is related to the stratigraphic sequence, which in turn, is related to the net advance. Note that it is assumed a decreasing salt supply rate and an increasing erosion rate (other parameters are not considered). B.1 to B.8: Models produced by the combination of the three control parameters. For each combination, the reduction of the salt supply rate and increase of the erosion rate is also expected, as these combinations are modifications of the ideal emplacement sequence previously represented. Next to each diagram, the expected stratigraphy architecture is indicated.

vertical wall, as it was previously hypothesized; 2) the extension of the Les Avellanes diapir is partly (or totally) related to a salt sheet deposit which extruded from a feeder area located northwest of the studied area; and 3) the diapir contact in the Os de Balaguer sequence, cannot be interpreted as a thrust, but as the base of an advancing salt sheet which was emplaced over the previous sedimentary sequence.

Finally, 8 conceptual models based on facies and stratigraphic architecture were built in order to evaluate the role of topography, sedimentation rate and salt dissolution on regard of the lateral advance of a salt sheet in continental settings. The proposed ideal succession shows a facies architecture characterized by an initial progradation, aggradation, and a final retrogradation. This sequence directly results from the advance, stagnation, and then retreat of the salt sheet front, assuming an increasing local erosion rate and a decreasing salt supply rate (Fig. 17A). The interplay of the controlling factors can favor or obstruct the salt advance (Fig. 17B), modifying the initial ideal sequence. Understanding the syn-kinematic sequence and the overall geometry of the salt contact, the controlling parameters can be narrowed down, and in consequence approximate the relative size and timing of the allochthonous salt emplacement.

Declaration of Competing Interest

The authors declare the following financial interests/personal relationships which may be considered as potential competing interests:

Gabriel Cofrade Rivas reports financial support was provided by University of Barcelona.

Data availability

Data will be made available on request.

Acknowledgments

This research was performed within the framework of DGICYT Spanish Project PGC2018-093903-B-C22, the research project Structure and Deformation of Salt-bearing Rifted Margins (SABREM), PID2020-117598GB-I00, funded by MCIN/ AEI /10.13039/501100011033, and PID2021-122467NB-C22 by Ministerio de Ciencia, Innovación y Universidades/Agencia Estatal de Investigación/Fondo Europeo de Desarrollo Regional and the Catalan Council to the Grup Consolidat de Recerca “Geologia Sedimentària” (2017SGR-824). We thank two anonymous referees, as well as Dr. John W. Counts, for their constructive reviews, which improved the quality of the manuscript. We also thank Dra. Elisabet Playà for her help regarding the facies interpretations. The author G. C. also acknowledges the support of the UB scholarship PREDOC-UB19/20 5660400.

References

Alsop, G., Weinberger, R., Levi, T., Marco, S., 2016. Cycles of passive versus active diapirism recorded along an exposed salt wall. J. Struct. Geol. 84, 47–67. https://doi.org/10.1016/j.jsg.2016.01.008.

Alsop, G.I., Brown, J.P., Davison, I., Gibling, M.R., 2000. The geometry of drag zones adjacent to salt diapirs. J. Geol. Soc. 157 (5), 1019–1029. https://doi.org/10.1144/jgs.157.5.1019.

Andrie, J.R., Giles, K.A., Lawton, T.F., Rowan, M.G., 2012. Halokinetic-sequence stratigraphy, fluvial sedimentology and structural geometry of the Eocene Carroza Formation along La Popa salt weld, La Popa Basin, Mexico. Geol. Soc. Lond., Spec. Publ. 363 (1), 59–79. https://doi.org/10.1144/sp363.4.

Angrand, P., Mouthereau, F., 2021. Evolution of the Alpine orogenic belts in the Western Mediterranean region as resolved by the kinematics of the Europe-Africa diffuse plate boundary. BSGF - Earth Sciences Bulletin 192, 42. https://doi.org/10.1051/bsgf/2021031.

Aref, M.A., Mannaa, A.A., 2021. The significance of gypsum morphology in interpreting environmental changes caused by human construction, Red Sea coastal evaporation environment, Saudi Arabia. Environ. Earth Sci. 80 (2) https://doi.org/10.1007/s12665-020-09298-4.

Arnal, I., Rovira, F.C., Márquez, L., Aliaga, A.M., de Porta, N.S., 2002. La plataforma carbonatada epeírica (Formaciones Imón e Isábena) del Triásico superior del Noreste de la Península Ibérica. Acta Geológica Hispánica 37 (4), 299–328.

Azambre, B., Rossy, M., Lago, M., 1987. Caractéristiques petrològiques des dolérites tholéiitiques d’âge triasique (ophites) du domaine pyrénéen. Bulletin de Minéralogie 110 (4), 379–396.

Basyoni, M.H., Aref, M.A., 2015. Sediment characteristics and microfacies analysis of Jizan supratidal sabkha, Red Sea coast, Saudi Arabia. Arabian Journal of Geosciences 8 (11), 9973–9992. https://doi.org/10.1007/S12517-015-1852-1.

Beamud, E., Muñoz, J.A., Fitzgerald, P.G., Baldwin, S.L., Garcés, M., Cabrera, L., Metcalf, J.R., 2010. Magnetostratigraphy and detrital apatite fission track thermochronology in syntectonic conglomerates: constraints on the exhumation of the South-Central Pyrenees. Basin Res. 23 (3), 309–331. https://doi.org/10.1111/j.1365-2117.2010.00492.x.

Beaumont, C., Muñoz, J.A., Hamilton, J., Fullsack, P., 2000. Factors controlling the Alpine evolution of the Central Pyrenees inferred from a comparison of observations and geodynamical models. Journal of Geophysical Research: Solid Earth 105 (B4), 8121–8145. https://doi.org/10.1029/1999jb900390.

Blair, C.T., McPherson, G.J., 1994. Alluvial fans and their natural distinction from rivers based on morphology, hydraulic processes, sedimentary processes, and facies assemblages. SEPM Journal of Sedimentary Research 64A, 450–489. https://doi.org/10.1306/d4267dde-2b26-11d7-8648000102c1865d.

Burrel, L., Teixell, A., 2021. Contractional salt tectonics and role of pre-existing diapiric structures in the Southern Pyrenean foreland fold–thrust belt (Montsec and Serres Marginals). J. Geol. Soc. 178 (4) https://doi.org/10.1144/jgs2020-085 jgs2020-085.

Callot, J.P., Trocmé, V., Letouzey, J., Albouy, E., Jahani, S., Sherkati, S., 2012. Pre-existing salt structures and the folding of the Zagros Mountains. Geol. Soc. Lond., Spec. Publ. 363 (1), 545–561. https://doi.org/10.1144/sp363.27.

Callot, J.P., Ribes, C., Kergaravat, C., Bonnel, C., Temiz, H., Poisson, A., Vrielynck, B., Salel, J.F., Ringenbach, J.C., 2014. Salt tectonics in the Sivas basin (Turkey): crossing salt walls and minibasins. Bulletin de la Société Géologique de France 185 (1), 33–42. https://doi.org/10.2113/gssgfbull.185.1.33.

Calvet, F., 1996. Estratigrafia del Triàsic de l’àrea de Les Avellanes. Servei Geològic de Catalunya (informe inédito). 35p.

Calvet, F., Márquez, L., Trifonova, E., 1994. Litoestratigrafía y bioestratigrafía (foraminíferos) de las facies Muschelkalk del Triásico Sudpirenaico y del Pirineo Vasco (España). Boletín Real Sociedad Española de Historia Natural (Sección Geología) 89, 167–188.

Calvet, F., Anglada, E., Salvany, J.M., 2004. El Triásico de los Pirineos. In: Vera, J.A. (Ed.), Geología de España (272–274). Sociedad Geológica de España and Instituto Geológico y Minero de España.

Calvet, M., Gunnell, Y., Laumonier, B., 2021. Denudation history and palaeogeography of the Pyrenees and their peripheral basins: an 84-million-year geomorphological perspective. Earth Sci. Rev. 215, 103436 https://doi.org/10.1016/j.earscirev.2020.103436.

Camara, P., Flinch, J., 2017. The Southern Pyrenees: A salt-based fold and thrust belt. In: Soto, J.I., Flinch, J.F., Tari, G. (Eds.), Permo-Triassic Salt Provinces of Europe, North Africa and the Atlantic Margins. Elsevier. Tectonics and Hydrocarbon Potential, pp. 395–415. https://doi.org/10.1016/B978-0-12-809417-4.00019-7.

Carola, E., Muñoz, J.A., Roca, E., 2015. The transition from thick-skinned to thin-skinned tectonics in the Basque-Cantabrian Pyrenees: the Burgalesa Platform and surroundings. Int. J. Earth Sci. 104 (8), 2215–2239. https://doi.org/10.1007/s00531-015-1177-z.

Carola, E., Ferrer, O., Vidal-Royo, O., Muñoz, J.A., 2017. Interpretation of salt-cored frontal structures in the Southern Pyrenees guided by analog modeling, surface and subsurface data. Interpretation 5 (1), 39–54.

Caus, E., Gómez-Garrido, A., 2015. Upper cretaceous biostratigraphy of the South-Central Pyrenees (Lleida, Spain). Geodin. Acta 3 (3), 221–228. https://doi.org/10.1080/09853111.1989.11105188.

Counts, J.W., Dalgarno, C.R., Amos, K.J., Hasiotis, S.T., 2019. Lateral Facies Variability along the margin of an Outcropping Salt-Withdrawal Minibasin, South Australia. J. Sediment. Res. 89 (1), 28–45. https://doi.org/10.2110/jsr.2019.2.

Cruset, D., Vergés, J., Albert, R., Gerdes, A., Benedicto, A., Cantarero, I., Travé, A., 2020. Quantifying deformation processes in the SE Pyrenees using U–Pb dating of fracture-filling calcites. J. Geol. Soc. 177 (6), 1186–1196. https://doi.org/10.1144/jgs2020-014.

Cuevas, J.L., 1989. La Formación Talarn: Estudio estratigráfico y sedimentológico de las fácies de un sistema aluvial en el tránsito Mesozoico-Cenozoico de la Conca de Tremp. Tesis de Licenciatura, Univ, de Barcelona.

Davoudi, A., Khodabakhsh, S., Rafiei, B., 2019. Alluvial fan facies of the Qazvin Plain: paleoclimate and tectonic implications during Quaternary. Geopersia 10 (1), 65–87. https://doi.org/10.22059/GEOPE.2019.277922.648469.

De Meer, S., Spiers, C., Peach, C., 1997. Pressure solution creep in gypsum: evidence for precipitation reaction control. Phys. Chem. Earth 22 (1–2), 33–37. https://doi.org/10.1016/s0079-1946(97)00074-8.

Dooley, T.P., Hudec, M.R., 2020. Extension and inversion of salt-bearing rift systems. Solid Earth 11 (4), 1187–1204. https://doi.org/10.5194/se-11-1187-2020.

Dooley, T.P., Jackson, M.P., Hudec, M.R., 2009. Inflation and deflation of deeply buried salt stocks during lateral shortening. J. Struct. Geol. 31 (6), 582–600. https://doi.org/10.1016/j.jsg.2009.03.013.

Duffy, O.B., Dooley, T.P., Hudec, M.R., Jackson, M.P., Fernandez, N., Jackson, C.A.L., Soto, J.I., 2018. Structural evolution of salt-influenced fold-and-thrust belts: A synthesis and new insights from basins containing isolated salt diapirs. J. Struct. Geol. 114, 206–221. https://doi.org/10.1016/j.jsg.2018.06.024.

Fillon, C., Gautheron, C., van der Beek, P., 2013. Oligocene–Miocene burial and exhumation of the Southern Pyrenean foreland quantified by low-temperature thermochronology. J. Geol. Soc. 170 (1), 67–77. https://doi.org/10.1144/jgs2012-051.

Fitzgerald, P., Muñoz, J.A., Coney, P., Baldwin, S., 1999. Asymmetric exhumation across the Pyrenean orogen: implications for the tectonic evolution of a collisional orogen. Earth Planet. Sci. Lett. 173 (3), 157–170. https://doi.org/10.1016/s0012-821x(99)00225-3.

Fletcher, R.C., Hudec, M.R., &. Watson, I. A., 1995. Salt glacier and composite sediment-salt glacier models for the emplacement and early burial of allochthonous salt sheets. In: Jackson, M.P.A., Roberts, D.G., Snelson, S. (Eds.), Salt Tectonics: A Global Perspective: AAPG Memoir, vol. 65, pp. 77–108.

Galdos, R., Canals, A., Cardellach, E., Perona, J., 2019. Tourmaline records the hydrothermal events related to Zn-Pb mineralization around the Murguía diapir (Basque Cantabrian Basin, N Spain). Geol. Acta 17 (5), 1–9. https://doi.org/10.1344/GeologicaActa2019.17.5.

Garcés, M., López-Blanco, M., Valero, L., Beamud, E., Muñoz, J.A., Oliva-Urcia, B., Vinyoles, A., Arbués, P., Cabello, P., Cabrera, L., 2020. Paleogeographic and sedimentary evolution of the south Pyrenean foreland basin. Mar. Pet. Geol. 113, 104105 https://doi.org/10.1016/j.marpetgeo.2019.104105.

Garcia-Castellanos, D., Vergés, J., Gaspar-Escribano, J., Cloetingh, S., 2003. Interplay between tectonics, climate, and fluvial transport during the Cenozoic evolution of the Ebro Basin (NE Iberia). Journal of Geophysical Research: Solid Earth 108 (B7). https://doi.org/10.1029/2002jb002073.

Giles, K.A., Rowan, M.G., 2012. Concepts in halokinetic-sequence deformation and stratigraphy. Geol. Soc. Lond., Spec. Publ. 363 (1), 7–31. https://doi.org/10.1144/sp363.2.

Graham, R., Jackson, M., Pilcher, R., Kilsdonk, B., 2012. Allochthonous salt in the sub-Alpine fold–thrust belt of Haute Provence, France. Geol. Soc. Lond., Spec. Publ. 363 (1), 595–615. https://doi.org/10.1144/sp363.30.

Grool, A.R., Ford, M., Vergés, J., Huismans, R.S., Christophoul, F., Dielforder, A., 2018. Insights into the crustal-scale dynamics of a doubly vergent orogen from a quantitative analysis of its forelands: a case study of the Eastern Pyrenees. Tectonics 37 (2), 450–476. https://doi.org/10.1002/2017tc004731.

Hearon IV, T.E., Rowan, M.G., Giles, K.A., Kernen, R.A., Gannaway, C.E., Lawton, T.F., Fiduk, J.C., 2015. Allochthonous salt initiation and advance in the northern Flinders and eastern Willouran ranges, South Australia: using outcrops to test subsurface-based modelsfrom the northern Gulf of Mexico. AAPG Bull. 99 (02), 293–331. https://doi.org/10.1306/08111414022.

Hudec, M.R., Jackson, M.P., 2006. Advance of allochthonous salt sheets in passive margins and orogens. AAPG Bull. 90 (10), 1535–1564. https://doi.org/10.1306/05080605143.

Hudec, M.R., Jackson, M.P., 2007. Terra infirma: understanding salt tectonics. Earth Sci. Rev. 82 (1–2), 1–28. https://doi.org/10.1016/j.earscirev.2007.01.001.

Hudec, M.R., Jackson, M.P., 2009. Interaction between spreading salt canopies and their peripheral thrust systems. J. Struct. Geol. 31 (10), 1114–1129. https://doi.org/10.1016/j.jsg.2009.06.005.

Huyghe, D., Mouthereau, F., Emmanuel, L., 2012. Oxygen isotopes of marine mollusc shells record Eocene elevation change in the Pyrenees. Earth Planet. Sci. Lett. 345–348, 131–141. https://doi.org/10.1016/j.epsl.2012.06.035.

Institut Cartogràfic de Catalunya, 2010. Mapa geològic de Catalunya, [Os de Balaguer 327–2-2 (64–26)]. 1:25.000, 1a edició. Cartografia geològica GT I, Barcelona. ISBN 841-47-745-0054-3.

Institut Cartogràfic de Catalunya, 2014. Mapa geològic de Catalunya, [Camarasa 328-1-2 (65-26)]. 1:25.000, 1a edició. Cartografia geològica GT I, Barcelona (ISBN 978-84-393-9128-9.).

Jackson, M., Hudec, M., 2017a. Salt Sheets and Salt Canopies. In: Salt Tectonics: Principles and Practice. Cambridge University Press, Cambridge, pp. 119–154. https://doi.org/10.1017/9781139003988.019.

Jackson, M., Hudec, M., 2017b. Special Topics in Seismic Interpretation of Salt Canopies. In: Salt Tectonics: Principles and Practice. Cambridge University Press, Cambridge, pp. 399–423. https://doi.org/10.1017/9781139003988.019.

Jackson, M., Warin, O., Woad, G., Hudec, M., 2003. Neoproterozoic allochthonous salt tectonics during the Lufilian orogeny in the Katangan Copperbelt, Central Africa. Geol. Soc. Am. Bull. 115, 314–330.

Koyi, H., 1998. The shaping of salt diapirs. J. Struct. Geol. 20 (4), 321–338. https://doi.org/10.1016/s0191-8141(97)00092-8.

Lagabrielle, Y., Labaume, P., de Saint Blanquat, M., 2010. Mantle exhumation, crustal denudation, and gravity tectonics during cretaceous rifting in the Pyrenean realm (SW Europe): Insights from the geological setting of the lherzolite bodies. Tectonics 29 (4), n/a. https://doi.org/10.1029/2009tc002588.

Lago, S.J., Galé-Bomao, C., Arranz-Yagüe, E., Vaquer-Navarro, R., GilImaz, A., Pocovi, A. J., 2000. Triassic tholeiitic dolerites (ophites) of the El Grado diapir (Pyrenees, Huesca, Spain) emplacement and composition. Estudios Geol. 56 (1–2), 3–18.

Lanaja, J.M., 1987. Contribución de la exploración petrolífera al conocimiento de la geología de España. IGME and Universidad Politécnica de Madrid. ISBN 8474743982.

Legeay, E., Ringenbach, J.C., Kergaravat, C., Pichat, A., Mohn, G., Vergés, J., Kavak, S.K., Callot, J.P., 2019. Structure and kinematics of the Central Sivas Basin (Turkey): salt deposition and tectonics in an evolving fold-and-thrust belt. Geological Society, London, Special Publications. https://doi.org/10.1144/SP490-2019-92. SP490–2019-92.

Li, J., Webb, A.A.G., Mao, X., Eckhoff, I., Colón, C., Zhang, K., Wang, H., Li, A., He, D., 2014. Active surface salt structures of the western Kuqa fold-thrust belt, northwestern China. Geosphere 10 (6), 1219–1234. https://doi.org/10.1130/ges01021.1.

López-Gómez, J., Alonso-Azcárate, J., Arche, A., Arribas, J., Fernández Barrenechea, J., Borruel-Abadía, V., Bourquin, S., Cadenas, P., Cuevas, J., de la Horra, R., Díez, J.B., Escudero-Mozo, M.J., Fernández-Viejo, G., Galán-Abellán, B., Galé, C., Gaspar-Escribano, J., Gisbert Aguilar, J., Gómez-Gras, D., Goy, A., Viseras, C., 2019. Permian-Triassic rifting stage. The Geology of Iberia: A Geodynamic Approach 29–112. https://doi.org/10.1007/978-3-030-11295-0_3.

Lopez-Mir, B., Muñoz, J.A., García Senz, J., 2014. Restoration of basins driven by extension and salt tectonics: example from the Cotiella Basin in the Central Pyrenees. J. Struct. Geol. 69, 147–162. https://doi.org/10.1016/j.jsg.2014.09.022.

McGuinness, D.B., Hossack, J.R., 1993. The development of allochthonous salt sheets as controlled by the rates of extension, sedimentation, and salt supply. In: Society of Economic Paleontologists and Mineralogists Gulf Coast Section, 14th Annual Research Conference, Extended Abstracts, pp. 127–139.

Muñoz, J.A., 1992. Evolution of a continental collision belt: ECORS-Pyrenees crustal balanced cross-section. https://doi.org/10.1007/978-94-011-3066-0_21.

Muñoz, J.A., Beamud, E., Fernández, O., Arbués, P., Dinarès-Turell, J., Poblet, J., 2013. The Ainsa Fold and thrust oblique zone of the Central Pyrenees: Kinematics of a curved contractional system from paleomagnetic and structural data. Tectonics 32 (5), 1142–1175. https://doi.org/10.1002/tect.20070.

Muñoz, J.A., Mencos, J., Roca, E., Carrera, N., Gratacós, O., Ferrer, O., Fernández, O., 2018. The Structure of the South-Central-Pyrenean fold and thrust belt as constrained by subsurface data. Geol. Acta 16 (4), 439–460. https://doi.org/10.1344/GeologicaActa2018.16.4.7.

Nikolinakou, M.A., Heidari, M., Hudec, M.R., Flemings, P.B., 2019. Stress and deformation in plastic mudrocks overturning in front of advancing salt sheets; implications for system kinematics and drilling. Rock Mech. Rock. Eng. 52 (12), 5181–5194. https://doi.org/10.1007/s00603-019-01852-2.

Peel, F.J., Travis, C.J., Hossack, J.R., 1995. Genetic structural provinces and salt tectonics of the Cenozoic offshore U.S. Gulf of Mexico: A preliminary analysis. In: Jackson, M.P.A., Roberts, D.G., Snelson, S. (Eds.), Salt Tectonics, A Global Perspective, AAPG Memoir, vol. 65, pp. 153–175.

Peel, F.J., Hudec, M.R., Weijermars, R., 2020. Salt diapir downbuilding: Fast analytical models based on rates of salt supply and sedimentation. J. Struct. Geol. 141, 104–202. https://doi.org/10.1016/j.jsg.2020.104202.

Pichat, A., Hoareau, G., Callot, J.P., Ringenbach, J.C., 2019. Characterization of Oligo-Miocene evaporite-rich minibasins in the Sivas Basin, Turkey. Marine and Petroleum Geology 110, 587–605. https://doi.org/10.1016/j.marpetgeo.2019.07.050.

Pichel, L.M., Finch, E., Huuse, M., Redfern, J., 2017. The influence of shortening and sedimentation on rejuvenation of salt diapirs: A new Discrete-Element Modelling approach. J. Struct. Geol. 104, 61–79. https://doi.org/10.1016/j.jsg.2017.09.016.

Pocoví, A., 1978. Estudio geológico de las Sierras Marginales Catalanas (Prepirineo de Lérida). Tesis Doctoral, Univ, de Barcelona.

Pujalte, V., Baceta, J., Schmitz, B., Orue-Echebarría, X., Payros, A., Bernaola, G., Apellaniz, E., Caballero, F., Robador, A., Serra-Kiel, J., Tosquella, J., 2009. Redefinition of the Ilerdian Stage (early Eocene). Geol. Acta 7 (1–2), 177–194. https://doi.org/10.1344/105.000000268.

Reuning, L., Johannes, S., Ansgar, H., Urai, J.L., Littke, R., Kukla, P.A., Rawahi, Z., 2009. Constraints on the diagenesis, stratigraphy and internal dynamics of the surface-piercing salt domes in the Ghaba Salt Basin (Oman): a comparison to the ARA Group in the South Oman Salt Basin. GeoArabia 14 (3), 83–120. https://doi.org/10.2113/geoarabia140383.

Ribes, C., Kergaravat, C., Crumeyrolle, P., Lopez, M., Bonnel, C., Poisson, A., Kavak, K.S., Callot, J.P., Ringenbach, J.C., 2016. Factors controlling stratal pattern and facies distribution of fluvio-lacustrine sedimentation in the Sivas mini-basins, Oligocene (Turkey). Basin Res. 29, 596–621. https://doi.org/10.1111/bre.12171.

Roca, E., Ferrer, O., Rowan, M.G., Muñoz, J.A., Butillé, M., Giles, K.A., Arbués, P., Matteis, M., 2021. Salt tectonics and controls on halokinetic-sequence development of an exposed Deepwater diapir: the Bakio Diapir, Basque-Cantabrian Basin, Pyrenees. Marine and Petroleum Geology 123, 104770. https://doi.org/10.1016/j.marpetgeo.2020.104770.

Rosell-Llompart, J., 2001. El Garumniense prepirenaico. Rev. Soc. Geol. España 14 (1–2), 47–56.

Roure, F., Choukroune, P., 1998. Contribution of the Ecors seismic data to the Pyrenean geology: Crustal architecture and geodynamic evolution of the Pyrenees. In: Damotte, B. (Ed.), The ECORS Pyrenean Deep Seismic Surveys, 1985–1994. Mém. Soc. Géol., France, pp. 37–52.

Rowan, M., 2017. An overview of allochthonous salt tectonics. In: Juan, Soto, Flinch, Joan, Tari, Gabor (Eds.), Permo-Triassic Salt Provinces of Europe, North Africa and the Atlantic Margins: Tectonics and Hydrocarbon Potential, pp. 97–114. https://doi.org/10.1016/b978-0-12-809417-4.00005-7.

Rowan, M.G., Hearon IV, T.E., Kernen, R.A., Giles, K.A., Gannaway-Dalton, C.E., Williams, N.J., Fiduk, J.C., Lawton, T.F., Hannah, P.T., Fischer, M.P., 2019a. A review of allochthonous salt tectonics in the Flinders and Willouran ranges, South Australia. Australian Journal of Earth Sciences 67 (6), 787–813. https://doi.org/10.1080/08120099.2018.1553063Rowan.

Rowan, M.G., Urai, J.L., Fiduk, J.C., Kukla, P.A., 2019b. Deformation of intrasalt competent layers in different modes of salt tectonics. Solid Earth 10 (3), 987–1013. https://doi.org/10.5194/se-10-987-2019.

Rowan, M.G., Krzywiec, P., Bukowski, K., Przybylop, J., 2020a. Nature and origin of large-scale and intrasalt deformation within the Wieliczka salt mine. Poland. Geological Quarterly 64 (4). https://doi.org/10.7306/gq.1557.

Rowan, M.G., Muñoz, J.A., Giles, K.A., Roca, E., Hearon, T.E., Fiduk, J.C., Ferrer, O., Fischer, M.P., 2020b. Folding and fracturing of rocks adjacent to salt diapirs. J. Struct. Geol. 141, 104187 https://doi.org/10.1016/j.jsg.2020.104187.

Rowan, M.G., Muñoz, J.A., Roca, E., Ferrer, O., Santolaria, P., Granado, P., Snidero, M., 2022. Linked detachment folds, thrust faults, and salt diapirs: Observations and analog models. J. Struct. Geol. 155, 104509 https://doi.org/10.1016/j.jsg.2022.104509.

Saleh, S., Williams, K.E., Rizvi, A., 2013. Rubble zone below salt: Identification and best drilling practices. In: Society of Petroleum Engineers Annual Technical Conference and Exhibition, paper SPE 166115, p. 17.

Salvany, J.M., 1999. Diapirismo triásico antiguo y reciente en el Anticlinal de Canelles, Sierras Marginales Catalanas (zona surpirenaica central). Rev. Soc. Geol. España 12 (2), 149–164.

Salvany, J.M., 2017. Las formaciones yesíferas del Triásico Superior y Jurásico Inferior de Camarasa, en el frente Surpirenaico Catalán. Estudios Geológicos 73 (2), e070. https://doi.org/10.3989/egeol.42914.460.

Salvany, J.M., Bastida, J.C., 2004. Análisis litoestratigráfico del Keuper Surpirenaico Central. Rev. Soc. Geol. España 17 (1–2), 3–26.

Sans, M., 2003. From thrust tectonics to diapirism. The role of evaporites in the kinematic evolution of the eastern south Pyrenean front. Geol. Acta 1 (3), 239–259.

Santolaria, P., Casas-Sainz, A.M., Soto, R., Pinto, V., Casas, A., 2014. The Naval diapir (southern Pyrenees): Geometry of a salt wall associated with thrusting at an oblique ramp. Tectonophysics 637, 30–44. https://doi.org/10.1016/j.tecto.2014.09.008.

Santolaria, P., Casas-Sainz, A.M., Soto, R., Casas, A., 2016. Gravity modelling to assess salt tectonics in the western end of the South Pyrenean Central Unit. J. Geol. Soc. 174 (2), 269–288. https://doi.org/10.1144/jgs2016-027.

Santolaria, P., Ferrer, O., Rowan, M., Snidero, M., Carrera, N., Granado, P., Muñoz, J.A., Roca, E., Schneider, C., Piña, A., Zamora, G., 2021. Influence of preexisting salt diapirs during thrust wedge evolution and secondary welding: Insights from analog modeling. J. Struct. Geol. 149, 104374 https://doi.org/10.1016/j.jsg.2021.104374.

Sarkarinejad, K., Sarshar, M.A., Adineh, S., 2018. Structural, micro-structural and kinematic analyses of channel flow in the Karmostaj salt diapir in the Zagros foreland folded belt, Fars province, Iran. Journal of Structural Geology 107, 109–131. https://doi.org/10.1016/j.jsg.2017.12.005.

Saura, E., Ardèvol, I., Oró, L., Teixell, A., Vergés, J., 2016. Rising and falling diapirs, shifting depocenters, and flap overturning in the cretaceous Sopeira and Sant Gervàs subbasins (Ribagorça Basin, southern Pyrenees). Tectonics 35 (3), 638–662. https://doi.org/10.1002/2015tc004001.

Séguret, M., 1972. Étude tectonique des nappes et séries décollées de la partie centrale du versant sud des Pyrénées – caractère synsédimentaire, rôle de la compression et de la gravité. In: Série Géologie Structurale, vol. 2. Publications de l'Universite des Sciences et Techniques du Languedoc (USTELA), Montpellier, France, p. 155.

Serra-Kiel, J., Canudo, J.I., Dinarés, J., Molina, E., Ortiz, N., Pascual, J.O., Samsó, J.M., Tosquella, J., 1994. Cronoestratigrafía de los sedimentos marinos del Terciario inferior de la Cuenca de Graus-Tremp (Zona Central Surpirenaica). Rev. Soc. Geol. España 7 (3–4), 273–297.

Serra-Kiel, J., Hottinger, L., Caus, E., Drobne, K., Ferràndez, C., Jauhri, A.K., Less, G., Pavlovec, R., Pignatti, J., Samsó, J.M., Schaub, H., Sirel, E., Strougo, A., Tambareau, Y., Tosquella, J., Zakrevskaya, E., 1998. Larger foraminifera biostratigraphy of the Tethyan Paleocene and Eocene. Bulletin de la Société Géologique de France 169, 281–299.

Sherkati, S., Letouzey, J., Frizon De Lamotte, D., 2006. Central Zagros fold-thrust belt (Iran): New insights from seismic data, field observation, and sandbox modeling. Tectonics 25 (4), n/a. https://doi.org/10.1029/2004tc001766.

Sohn, Y.K., Rhee, C.W., Kim, B.C., 1999. Debris Flow and Hyperconcentrated Flood-Flow Deposits in an Alluvial Fan, Northwestern part of the cretaceous Yongdong Basin, Central Korea. The Journal of Geology 107 (1), 111–132. https://doi.org/10.1086/314334.

Talbot, C., Aftabi, P., 2004. Geology and models of salt extrusion at Qum Kuh, Central Iran. J. Geol. Soc. 161 (2), 321–334. https://doi.org/10.1144/0016-764903-102.

Talbot, C.J., 1998. Extrusions of Hormuz salt in Iran. Geol. Soc. Lond., Spec. Publ. 143 (1), 315–334. https://doi.org/10.1144/gsl.sp.1998.143.01.21.

Talbot, C.J., Pohjola, V., 2009. Subaerial salt extrusions in Iran as analogues of ice sheets, streams and glaciers. Earth Sci. Rev. 97 (1–4), 155–183. https://doi.org/10.1016/j.earscirev.2009.09.004.

Talbot, C.J., Medvedev, S., Alavi, M., Shahrivar, H., Heidari, E., 1999. Salt extrusion at Kuh-e-Jahani, Iran, from June 1994 to November 1997. Geol. Soc. Lond., Spec. Publ. 174 (1), 93–110. https://doi.org/10.1144/GSL.SP.1999.174.01.06.

Teixell, A., 1998. Crustal structure and orogenic material budget in the west Central Pyrenees. Tectonics 17 (3), 395–406. https://doi.org/10.1029/98tc00561.

Teixell, A., Barnolas, A., 1996. Mapa geológico de la Hoja n° 327 (Os de Balaguer). Mapa Geológico de España E. 1:50.000. Segunda Serie (MAGNA), Primera edición. IGME (Depósito legal: M-44051–2006. ISBN: 84-7840-652-2).

Teixell, A., Muñoz, J.A., 2000. Evolución tectono-sedimentaria del Pirineo meridional durante el Terciario: una síntesis basada en la transversal del río Noguera Ribagorçana. Rev. Soc. Geol. España 12 (2), 251–264.

Teixell, A., Labaume, P., Ayarza, P., Espurt, N., de Saint Blanquat, M., Lagabrielle, Y., 2018. Crustal structure and evolution of the Pyrenean-Cantabrian belt: A review and new interpretations from recent concepts and data. Tectonophysics 724-725, 146–170. https://doi.org/10.1016/j.tecto.2018.01.009.

Thomas, R.J., Ellison, R.A., Goodenough, K.M., Roberts, N.M.W., Allen, P.A., 2015. Salt domes of the UAE and Oman: probing Eastern Arabia. Precambrian Res. 256, 1–16. https://doi.org/10.1016/j.precamres.2014.10.011.

Ullastre, J., Masriera, A., 1999. Análisis estratigráfico del Paleógeno del sinclinal de Tragó de Noguera: su importancia en la geologia regional (Pirineo catalano-aragonés, España). Treballs del Museu de Geologia de Barcelona 8, 85–111.

Vergés, J., Muñoz, J.A., 1990. Thrust sequence in the southern Central Pyrenees. Bulletin de La Société Géologique de France VI (2), 265–271. https://doi.org/10.2113/gssgfbull.vi.2.265.

Vergés, J., Muñoz, J.A., Martínez, A., 1992. South Pyrenean fold and thrust belt: The role of foreland evaporitic levels in thrust geometry. In: McClay, K.R. (Ed.), Thrust Tectonics. Springer, Dordrecht. https://doi.org/10.1007/978-94-011-3066-0_23.

Vergés, J., Fernàndez, M., Martínez, A., 2002. The Pyrenean orogen: pre-, syn-, and post-collisional evolution. In: Rosenbaum, G., Lister, G.S. (Eds.), Reconstruction of the evolution of the Alpine-Himalayan Orogen. Journal of the Virtual Explorer, 8, pp. 55–74.

Warren, J.K., 1982. The hydrological setting, occurrence and significance of gypsum in late Quaternary salt lakes in South Australia. Sedimentology 29 (5), 609–637. https://doi.org/10.1111/j.1365-3091.1982.tb00071.x.

Warren, J.K., 2006. Salt Dissolution and Pointers to Vanished Evaporites: Karst, Breccia, Nodules and Cement. In: Evaporites: A geological compendium. Springer, Cham, pp. 613–761.

Warren, J.K., 2016. Sabkhas, saline mudflats and pans. In: Evaporites: A geological compendium. Springer, Cham, pp. 207–301.

Yu, X., Li, S., Li, S., 2018. Alluvial fan depositional system. In: Clastic Hydrocarbon Reservoir Sedimentology. Advances in Oil and gas Exploration & Production. Springer, Cham, pp. 325–351. https://doi.org/10.1007/978-3-319-70335-0_8.

Závada, P., Desbois, G., Urai, J., Schulmann, K., Rahmati, M., Lexa, O., Wollenberg, U., 2015. Impact of solid second phases on deformation mechanisms of naturally deformed salt rocks (Kuh-e-Namak, Dashti, Iran) and rheological stratification of the Hormuz Salt Formation. J. Struct. Geol. 74, 117–144. https://doi.org/10.1016/j.jsg.2015.02.009.

Závada, P., Bruthans, J., Adineh, S., Warsitzka, M., Zare, M., 2021. Composition and deformation patterns of the caprock on salt extrusions in southern Iran – Field study on the Karmostaj and Siah Taq diapirs. J. Struct. Geol. 151, 104422 https://doi.org/10.1016/j.jsg.2021.104422.